How do granitoid magmas mix with each other? Insights from textures, trace element and Sr-Nd isotopic composition of apatite and titanite from the Matok pluton (South Africa)

Author(s):
Laurent, Oscar; Zeh, Armin; Gerdes, Axel; Villaros, Arnaud; Gros, Katarzyna; Słaby, Ewa

CrossMark

ORIGINAL PAPER

How do granitoid magmas mix with each other? Insights from textures, trace element and Sr–Nd isotopic composition of apatite and titanite from the Matok pluton (South Africa)

Oscar Laurent[1,2,6] · Armin Zeh[1,3] · Axel Gerdes[1] · Arnaud Villaros[4] ·
Katarzyna Gros[5] · Ewa Słaby[5]

Abstract In plutonic systems, magma mixing is often modelled by mass balance based on whole-rock geochemistry. However, magma mixing is a chaotic process and chemical equilibration is controlled by non-linear diffusive–advective processes unresolved by the study of bulk samples. Here we present textural observations, LA-(MC-) ICP-MS trace element and Sr–Nd isotopic data of accessory apatites and titanites from a hybrid granodiorite of the Neoarchean Matok pluton (South Africa), collected in a zone of conspicuous mixing between mafic and felsic magmas. Apatite grains mostly show a pronounced zoning in CL images, corresponding to abrupt changes in REE and HFSE concentrations recording their transfer through compositionally different melt domains during mixing. These grains crystallized early, at temperatures of 950–1000 °C. Titanite grains crystallized at temperatures of 820–900 °C (Zr-in-sphene thermometry). They show limited intra-grain chemical variations but huge inter-grain compositional scatter in REE and HFSE, pinpointing crystallization within a crystal mush, from isolated melt pockets having different composition from one another owing to incomplete chemical homogenization and variable Rayleigh fractionation. These chemical–textural characteristics, in combination with partitioning models and Polytopic Vector Analysis, point to "self-mixing" between co-genetic dioritic and granodioritic/granitic magmas. Both resulted from differentiation of mantle-derived mafic melts, showing that mixing does not necessarily involve magmas from contrasted (crust vs. mantle) sources. Systematic variations in εNd_t (−4.5 to −2.5) and $^{87}Sr/^{86}Sr_{(i)}$ (0.703–0.707) of titanite and apatite grains/domains crystallized from the two magmas point to an isotopically inhomogeneous mantle source, which is not resolved by bulk-rock isotopic data. Interaction between the two magmas must have occurred at relatively high temperatures (ca. 900°C) so that their viscosity contrast remained low, allowing efficient mechanical mixing. Despite this, chemical homogenization was incomplete, as recorded by diffusive fractionation between REE–HFSE and Sr. Modelling thereof reveals that chemical exchange between the liquid phases of the two mixed magmas did not last more than a few tens to hundreds of years. The chemical equilibration between mixed magmas thus strongly depends on the considered elements and observational length scales.

Communicated by Othmar Müntener.

✉ Oscar Laurent
oscarlaurent86@gmail.com

1 Facheinheit Mineralogie, Institut für Geowissenschaften, J.W. Goethe Universität, Altenhöferallee 1, 60438 Frankfurt am Main, Germany

2 Département de Géologie B20, Université de Liège, Quartier Agora, allée du six-Août 12, 4000 Liège, Belgium

3 Abteilung Mineralogie und Petrologie, Institut für Angewandte Geowissenschaften, Karlsruher Institut für Technologie, Campus Süd, Karlsruhe, Germany

4 Université d'Orléans, ISTO-BRGM-CNRS UMR 7327, Orléans, France

5 Institute of Geological Sciences, Polish Academy of Sciences, Twarda 51/55, 00-818 Warsaw, Poland

6 Present Address: Institute for Geochemistry and Petrology, ETH Zürich, Zurich, Switzerland

🖄 Springer

Introduction

The mixing of compositionally distinct magmas is a fundamental process on Earth (Wilcox 1999). It has long been considered as a trigger for explosive volcanic eruptions (e.g. Sparks et al. 1977; Druitt et al. 2012; Murphy et al. 1998; Ruprecht and Bachmann 2010) and could play a role in the formation of layered intrusions, related ore deposits (e.g. Vantongeren and Mathez 2013) as well as widespread, intermediate igneous rocks such as arc andesites (e.g. Bacon 1986; Eichelberger 2010; Reubi and Blundy 2009). In plutonic systems, magma mixing is widely documented by field evidence, such as microgranular mafic enclaves (MMEs) and composite dykes in granitoid plutons (Barbarin 2005; Didier and Barbarin 1991; Kemp 2004). The chemical variability of whole-rock sample populations in such systems (linear trends in binary plots) has often been interpreted as reflecting variable degrees of interactions between crust- and mantle-derived magmas (e.g. Barbarin 2005; Castro et al. 1990, 1991; Clemens et al. 2009, 2016; Janoušek et al. 2004; Karsli et al. 2010; Kemp 2004; Maas et al. 1997; Moyen et al. 2001; Słaby and Martin 2008; Wiebe et al. 2002, 2007 among many others). This would play a key role in the origin of "I-type", metaluminous to slightly peraluminous granitoid suites having chemical and isotopic characteristics intermediate between mantle and crustal end-members (Barbarin 1999; Castro et al. 1991; Kemp and Hawkesworth 2003).

However, the occurrence of magma mixing structures and chemical trends in granitoid plutons does neither necessarily imply that contrasted, crust- and mantle-derived magmas were involved (Bonin 2004; Pin et al. 1990; Wiebe et al. 2007), nor that large volumes of hybrid magmas were produced thereby (Clemens et al. 2009, 2016). The identification of end-members is complicated by the fact that isotopic evidence may be equivocal (Couzinié et al. 2016; Laurent et al. 2013a; Pin et al. 1990) and by the possible occurrence of other processes that would also result in linear trends in whole-rock sample populations (crystal accumulation; peritectic phase entrainment; restite unmixing) (Clemens et al. 2011; Farina et al. 2012; Laurent et al. 2013a; Villaros et al. 2009; Williamson et al. 1997). In addition, magma mixing is a process controlled by chaotic dynamics (Perugini and Poli 2012 and references therein). The chemical homogenization between two compositionally contrasted magmas requires efficient mechanical mixing and subsequent chemical equilibration by diffusion (Ottino 1989; Petrelli et al. 2011). Those parameters depend themselves on the viscosity contrast between the two magmas (Jellinek and Kerr 1999; Laumonier et al. 2014a, b; Poli et al. 1996; Sparks and Marshall 1986), the resulting wavelength of chemical heterogeneities (Petrelli et al. 2011; Spera et al. 2016) and the time spent by the system in the partially molten state (Oldenburg et al. 1989; Perugini and Poli 2012; Petrelli et al.

2006). In addition, groups of chemical elements such as REEs and LILEs have very contrasted diffusion behaviours in silicate melts (Zhang et al. 2010) resulting in "diffusive fractionation" processes during mixing (De Campos et al. 2011; Perugini et al. 2008, Perugini et al. 2012), i.e. non-linear chemical exchanges between the interacting magmas.

Clearly, all these processes cannot be accurately described by classical approaches based on mass balance and whole-rock compositions (Perugini et al. 2006; Perugini and Poli 2012). In contrast, recent studies have demonstrated that mineral phases grown during mixing show very clear textural and compositional variations, both at the crystal and at the sample scales: this includes alkali and plagioclase feldspars (Alves et al. 2009; Perugini et al. 2005; Pietranik and Koepke 2009; Słaby et al. 2008, 2010, 2011b, Słaby et al. 2017) as well as accessory phases like apatite and/or titanite (Bruand et al. 2014; Lisowiec et al. 2015; McLeod et al. 2011; Miles et al. 2013; Pietranik et al. 2011; Rao et al. 2012; Sun et al. 2010; Tepper and Kuehner 1999). The latter are of outstanding interest because (1) their trace element composition is very sensitive to the nature of the magma in which they crystallized, particularly in the case of apatite (Belousova et al. 2001; Chu et al. 2009; Miles et al. 2013; Sha and Chappell 1999); and (2) thanks to recent analytical development, Sr and/or Nd isotopic compositions can now be routinely analysed in situ by LA-MC-ICP-MS in these minerals (Fisher et al. 2011; Foster and Vance 2006; Vroon et al. 2008; Yang et al. 2014).

The ca. 2.68 Ga-old Matok pluton, from the northern Kaapvaal Craton in South Africa (Fig. 1), represents a well-documented suite of granitoids (Bohlender 1991; Barton et al. 1992; Laurent et al. 2013a, b, 2014a, c; Rapopo 2010; Zeh et al. 2009), which typically form linear trends between the compositions of mantle-derived and crust-derived magmas in binary diagrams (Fig. 2). There is, moreover, unambiguous field evidence supporting that coeval, mafic and felsic magmas interacted with each other to form hybrid granodiorites (Fig. 3). Altogether, this makes the Matok pluton an ideal case to better constrain the dynamics and importance of magma mixing in plutonic environments, especially through the study of accessory minerals in hybrid samples that, therefore, unequivocally grew during the process. The present paper accordingly presents a detailed investigation of accessory apatite and titanite from such a hybrid granodiorite of the Matok pluton, based on optical microscopy, cathodoluminescence (CL), back-scattered electron (BSE) imaging and LA-(MC-)ICP-MS analyses of trace element concentrations, Rb–Sr and Sm–Nd isotopic systems. The results will provide new information about: (1) how accessory apatite and titanite record magma mixing; (2) the nature of the two mixing end-members; (3) the physical conditions of mixing in terms of temperature and rheology; and (4) the extent and timescales of chemical equilibration.
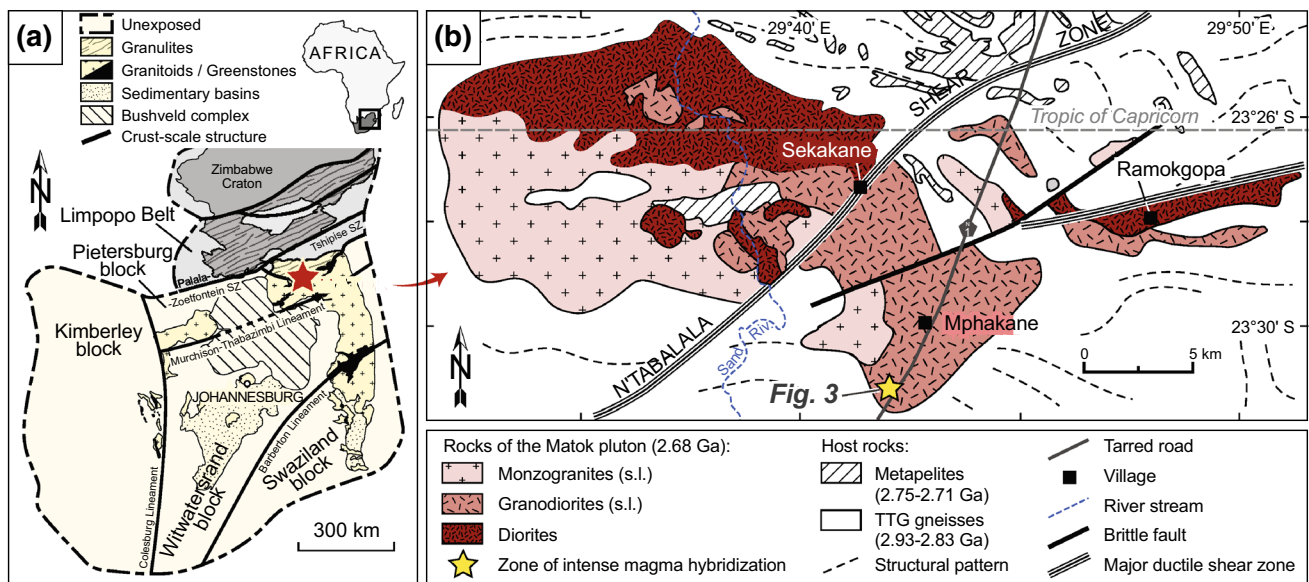
Fig. 1 **a** Schematic map of the Kaapvaal Craton showing the different crustal blocks and lineaments (after Eglington and Armstrong 2004). **b** Interpretative geological map of the Matok pluton (Laurent et al. 2014c after Bohlender 1991) showing the location of the "hybridization zone" (*yellow star*; see Fig. 3)
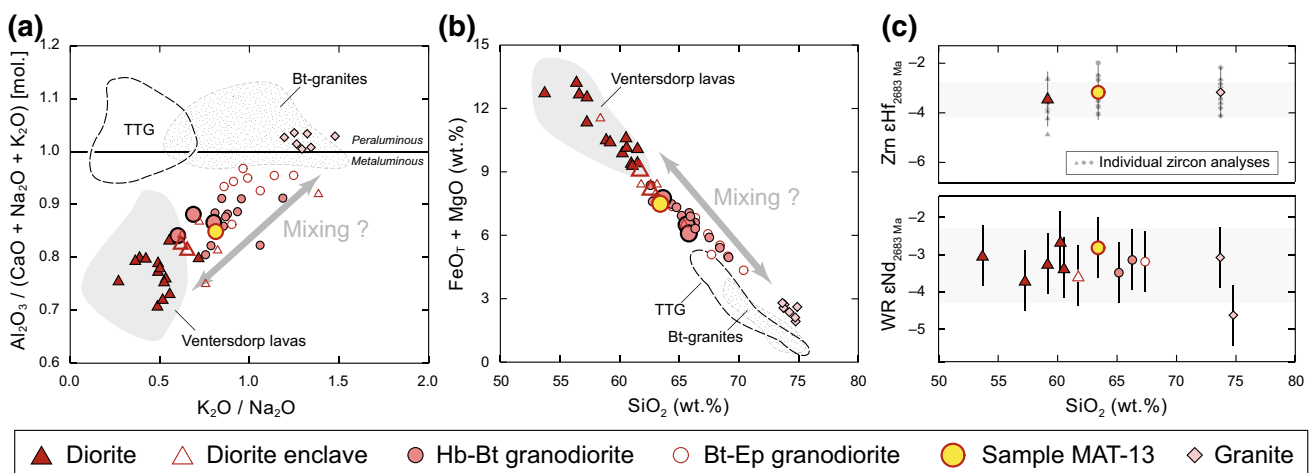

Fig. 2 Summary of available geochemical and isotopic data on the Matok pluton. Major-element composition of whole-rock samples (data from Laurent et al. 2014c) plotted in **a** molar Al_2O_3/($CaO + Na_2O + K_2O$) vs. K_2O/Na_2O and **b** $FeO_T + MgO$ vs. SiO_2 plots, showing the possible interpretation of the Matok granodiorites as hybrids between the mantle-derived, coeval) Ventersdorp lavas (data from Altermann and Lenhardt 2012; Crow and Condie 1988) and crust-derived, biotite-bearing granites from the PB (data from Laurent et al. 2014a). **c** Plot of zircon Hf isotopic compositions (*upper panel*; data from Laurent and Zeh 2015) and whole-rock Nd isotopic compositions (*lower panel*; data from Laurent et al. 2014c) of samples from the Matok pluton as a function of the bulk-rock SiO_2 content; the *grey field* corresponds to the average ± 2 SD. *Larger symbols* correspond to samples from the "hybridization zone"

The Matok pluton

The Matok pluton is intrusive in the Pietersburg Block (PB), the northernmost terrane of the Kaapvaal Craton in South Africa (Eglington and Armstrong 2004; Poujol et al. 2003; Zeh et al. 2009), which results from Meso-/Neoarchean crustal formation and accretion (2.97–2.68 Ga) in a convergent margin setting (see Laurent et al. 2014a; Laurent and Zeh 2015 and references therein). The Matok pluton is a ca. 250 km² magmatic complex, made up of diorites, granodiorites and granites (Fig. 1c) (Bohlender et al. 1992; Bohlender 1991; Laurent et al. 2014c; Rapopo 2010). A
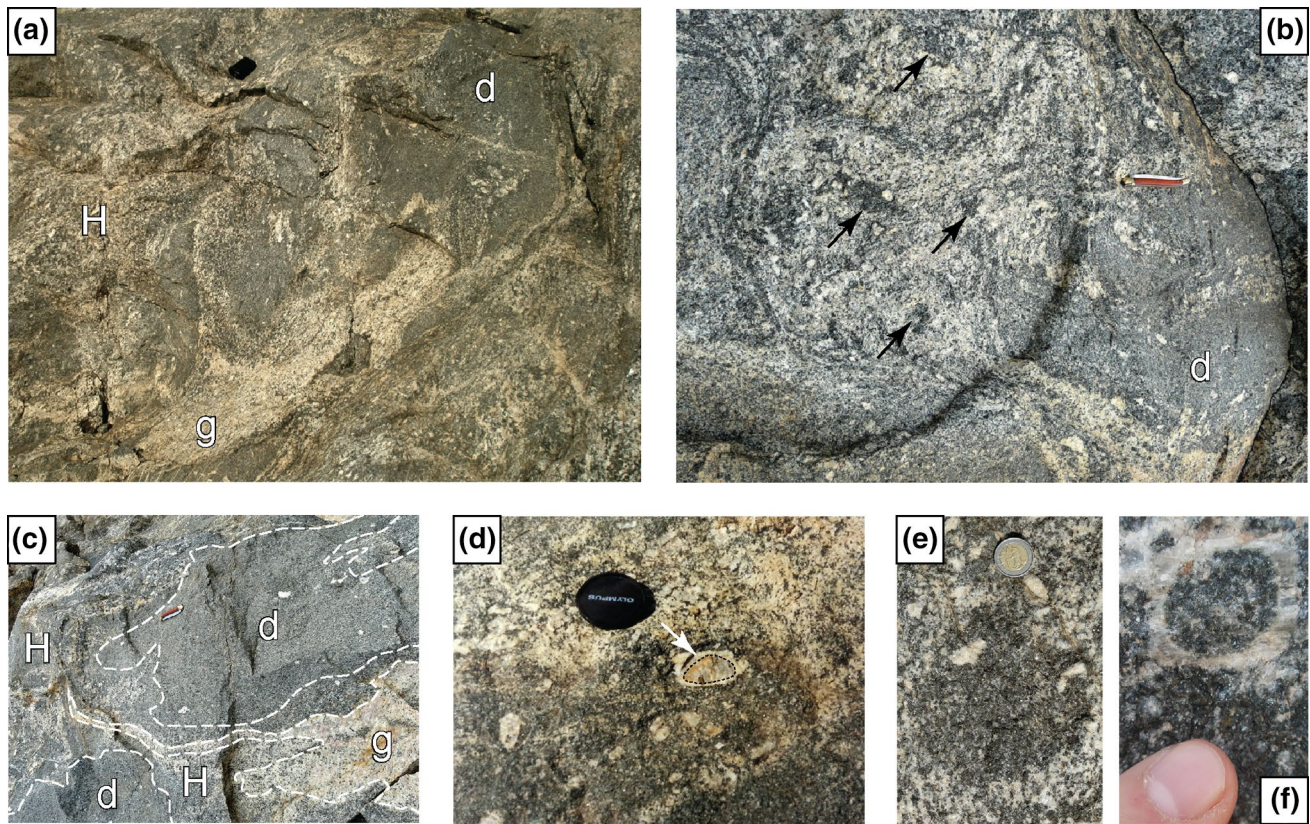
Fig. 3 Field pictures from the "hybridization zone" of the Matok pluton. **a** Outcrop-scale interaction between dioritic [*d*] and granitic [*g*] magmas, with diffuse to sharp contacts and formation of hybrid phases with spotted appearance [*H*] between the coherent domains (camera box for scale, ca. 10 × 5 cm). **b** Active mixing domains where the diorite [*d*] is disseminated in the felsic melt, forming stretched enclaves (*arrows*), schlieren and filament-like structures (*left-hand side of the picture*) (knife for scale, ca. 10 cm). **c** Coherent bodies of diorite [*d*] intruded by granite [*g*] and formation of hybrid granodiorite [*H*] at the contacts; the *dashed lines* out-line the approximate boundaries between the different phases (knife for scale, ca. 10 cm). **d** Detail of an irregular contact zone between diorite and hybrid granodiorite, including a feldspar phenocryst with a rapakivi texture (partly resorbed K-feldspar rimmed by plagioclase; *white arrow*) (from Bohlender 1991). **e** Globular enclave of dioritic material within a hybrid phase, containing K-feldspar phenocrysts from the host mechanically introduced in the enclave (coin for scale, ca. 2.5 cm). **f** Ocellus-like structure in a hybrid domain showing a rounded amphibole-, biotite- and epidote-rich core rimmed by quartz and K-feldspar

detailed description of these rocks has been given in earlier studies (Bohlender 1991; Bohlender et al. 1992; Barton et al. 1992; Laurent et al. 2014b, c; Rapopo 2010) and is summarized hereafter. Diorites are biotite- and either pyroxene- or amphibole-bearing, dark medium-grained rocks. The volumetrically dominant granodiorites are medium- to coarse-grained, sometimes porphyritic rocks that can be classified into two groups: biotite- ± amphibole-bearing; and biotite-, epidote- and titanite-bearing. Granites show various textures and grain sizes and contain limited amounts of biotite, if any. Owing to the occasional presence of orthopyroxene in diorites and granodiorites, the rocks of the Matok pluton were sometimes described as "charnockites" s.l. (Bohlender et al. 1992; Rajesh et al. 2014).

LA-ICP-MS zircon dating showed that the different phases have identical ages within uncertainty, from 2688 ± 8 to 2679 ± 9 Ma (Laurent et al. 2013b; Zeh et al. 2009), with an average of 2683.4 ± 3.4 Ma (weighted average of zircon $^{207}Pb/^{206}Pb$ ages from four samples; $n = 111$; MSWD = 0.61). Post-emplacement deformation occurred along discrete ductile shear zones (Bohlender et al. 1992; Kreissig et al. 2001; Laurent et al. 2014c) related to the 2690–2630 Ma Hout River Shear Zone (Kramers et al. 2014; Kreissig et al. 2001; Smit et al. 2014). Some rocks of the Matok pluton were hydrothermally altered along the shear zones (Bohlender 1991).

The rocks of the Matok pluton are metaluminous, medium- to high-K calc-alkaline and span a wide range in SiO$_2$ contents, showing a distinct composition from the regional TTG gneisses and granites (Fig. 2). Laurent et al. (2014c) showed that the Matok diorites were formed by fractionation from a mafic parent, derived from

the involvement of two distinct mantle sources: (1) a lithospheric mantle enriched in incompatible elements and (2) the asthenosphere.

Magma mixing in the Matok pluton

The composition of the Matok granodiorites is intermediate between two end-members (Fig. 2):

1. the Matok diorites, which have the same chemical composition as coeval, mafic volcanic rocks from the Ventersdorp supergroup (Altermann and Lenhardt 2012; Crow and Condie 1988);
2. the Matok granites, having affinities with local biotite granites derived from crustal melting (Laurent et al. 2014a, c).

The whole-rock geochemistry of the granodiorites could then result from a mixture between basaltic/andesitic (mantle-derived) and granitic (crust-derived) magmas (Fig. 2). The importance of magma mixing is supported by field relationships throughout the pluton (e.g. round diorite enclaves within more felsic rocks; Laurent et al. 2014c; Rapopo 2010), but more particularly in a hybridization zone covering a wide surface (>1.5 km^2) at its southernmost edge (Fig. 1c). Here, dark, medium-grained diorite is complexly mingled with lighter, grey to pink granite, forming hybrid granodioritic rocks with a characteristic "spotted" appearance (Fig. 3a, b). The six samples studied from this area by Laurent et al. (2014c) have typically intermediate compositions between diorites and granites (Fig. 2).

In the hybridization zone, the diorite is either mechanically disseminated in the felsic magma, forming dark schlieren, filament-like structures or swarms of small enclaves (Fig. 3b) or forms coherent bodies intruded by veins or patches of granite (Fig. 3c). These structures are very similar to those observed in numerical and experimental models of magma mixing (Laumonier et al. 2014a, b; Perugini et al. 2002, 2008, 2012; Petrelli et al. 2011). The contacts between diorite and granite are either irregular, gradational (Fig. 3a–c) or outlined by centimeter-thick biotite-rich selvedges. Rapakivi feldspars (Fig. 3c), MMEs with feldspar phenocrysts straddling their boundaries (Fig. 3d) and ocelli-like structures (quartz coronas around mafic aggregates; Fig. 3e) are frequent. These features of textural disequilibria also typically result from interactions between two compositionally different magmas (Perugini and Poli 2012).

Sample MAT-13 was selected to investigate the effect of magma mixing on the accessory apatite and titanite, because it has a representative composition for the hybridization zone

(Fig. 2). As typical for Matok hybrid rocks, sample MAT-13 is a medium-grained (0.1–1 cm) granodiorite showing the distinctive "spotted" appearance (see Fig. 3a, b). This results from mafic aggregates of irregular shapes and sizes (1–3 cm) enclosed within a leucocratic matrix. The aggregates consist of greenish–brownish biotite (1–5 mm), subhedral magmatic epidote and titanite (0.2–2 mm) (Fig. 4), occurring together with quartz, ilmenite, magnetite and locally amphibole. The leucocratic matrix is made up of pluri-millimetric, subhedral plagioclase crystals (ca. An$_{20}$; Rapopo 2010) having a bluish-green to greenish-brown colour in CL images (Fig. 4); together with quartz and anhedral K-feldspar (Fig. 4). The contact between the mafic and leucocratic domains is outlined by a fine-grained (<0.5 mm) intergrowth of epidote, biotite, quartz and albitic plagioclase (Ab$_{0-5}$; Rapopo 2010; Laurent 2012) having a reddish colour in CL images (Fig. 4).

Apatite, titanite and zircon are abundant accessory minerals, forming crystals up to 0.2–0.5 mm long. These phases mostly occur in the mafic aggregates, but also in the quartzofeldspathic domains, especially at grain boundaries or as inclusions in plagioclase in the case of apatite (Fig. 4). Apatite is very commonly included in titanite (Fig. 4).

Analytical methods

Image acquisition

Cathodoluminescence (CL) imaging was performed at the Polish Academy of Sciences (PAN) in Warsaw, on carbon-coated, polished thin sections using a hot cathode-equipped CL microscope (HC1-LM; Neuser et al. 1995) operated at 14 kV accelerating voltage and current density of ca. 10 µA mm^2. Luminescence images were captured online with a Peltier-cooled digital video camera (KAPPA 961-1138 CF 20 DXC). Further CL and BSE images were performed on apatites and titanites hand-picked from heavy mineral concentrates and set in 1-in. epoxy mounts, by scanning electron microscopy (SEM) at Goethe Universität Frankfurt (GUF), Germany, using a JEOL JSM-6490 instrument equipped with a Gatan MiniCL detector.

LA-ICP-MS trace element and isotopic analyses

The analyses of trace element contents, Rb–Sr and Sm–Nd isotopes in separated and mounted crystals of apatite and titanite were performed by laser ablation-(multi-collector-) sector field, inductively coupled mass spectrometry (LA-[MC-]SF-ICP-MS) at Goethe Universität Frankfurt (GUF). We used a RESOlution (ASI) 193-nm ArF Excimer laser, equipped with a two-volume Laurin Technic S-155 ablation

Fig. 4 Photomicrographs from sample MAT-13 obtained using a classical optical microscope (polarized light; *left-hand side*) and an optical microscope equipped with cathodoluminescence (*right-hand side*). *Ab* albite (<5% An), *Ap* apatite, *Bt* biotite, *Ep* epidote, *Kfs* K-feldspar, *Pl* plagioclase (>5% An), *Qz* quartz, *Ttn* titanite. *Scale bar* is 2 mm. See text for details
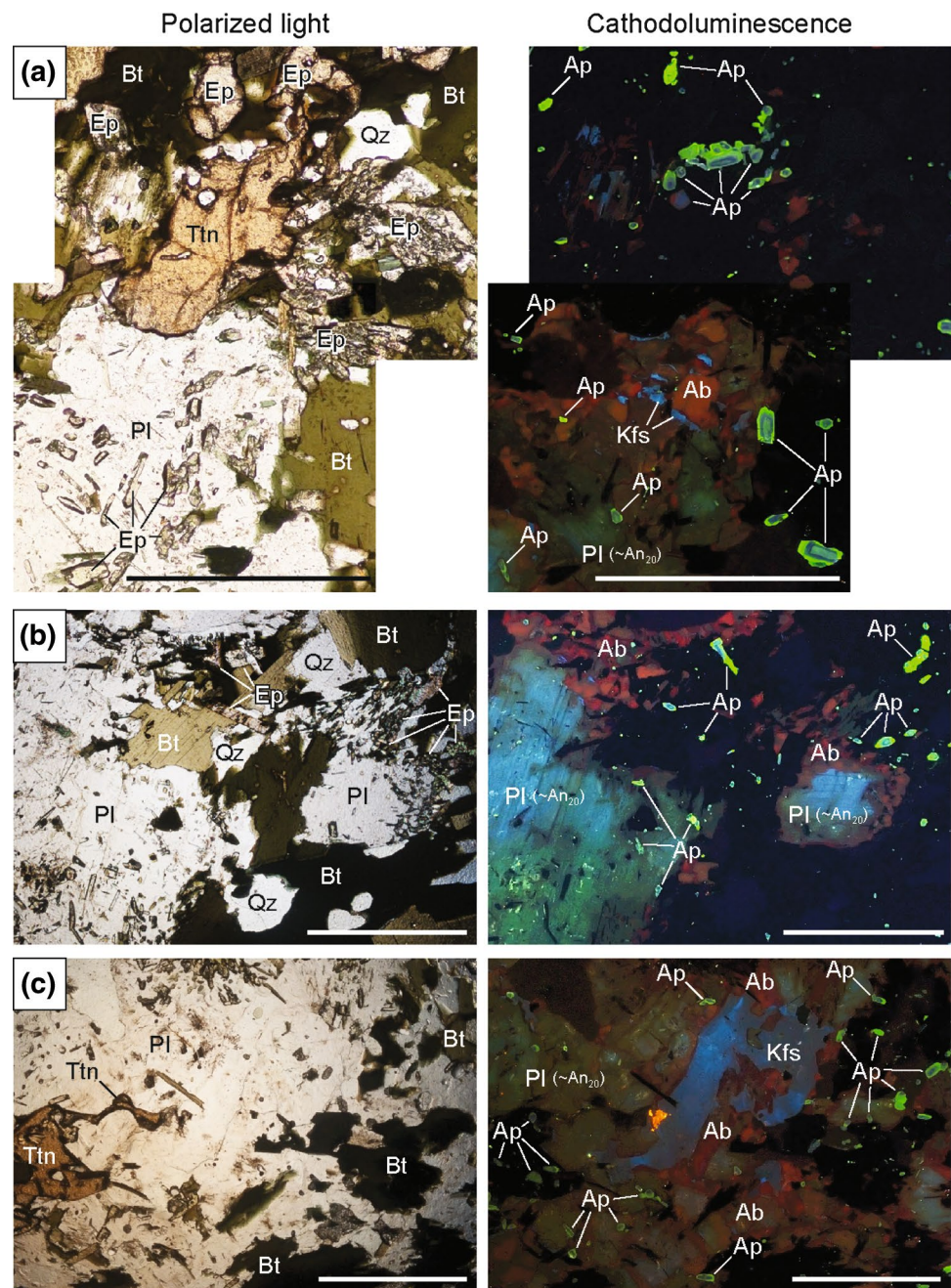
cell, coupled with a Thermo-Scientific ELEMENT 2 SF-ICP-MS for trace elements; and a Thermo-Finnigan Neptune multi-collector SF-ICP-MS for Rb–Sr and Sm–Nd isotopes.

For all measurements, ablation was performed in a He stream (0.6 L min^{-1}) to which were admixed high-purity N$_2$ (0.07 L min^{-1}) and sample gas (Ar at 0.7 L min^{-1}) downstream of the ablation cell. Post-ablation homogenization was performed for isotopic analyses using a Squid® tubing.

Specific conditions for each type of analyses (trace elements, Rb–Sr isotopes, Sm–Nd isotopes) are reported in the Supplementary Material, together with the results of analyses of reference materials (see Tables S2 and S3).

Results

Apatite textures and trace element composition

Optical CL images of apatites in thin sections reveal that the grains are characterized by three distinct colour domains which alternation defines complex zoning patterns (Fig. 5a, see also Fig. 4): (1) greenish to bluish-green luminescence,

Fig. 5 Representative examples of optical cathodoluminescence (CL) (**a**) and SEM-CL (**b–d**) images of apatites from MAT-13. In **b–d**, the position of LA-(MC-)ICP-MS spots for trace elements, Rb–Sr and Sm–Nd analyses are indicated, together with grain numbers. **a** Pictures of selected, zoned apatites grains and interpretation of the "G(greenish)-type", "B(bluish)-type" and "Y(yellowish)-type" domains. **b** Examples of homogeneous, "G-type" apatite grains; note the systematic presence of a thin "B-type" ring close to the edge of the crystals. **c** Examples of zoned apatites; the bright-CL domains correspond to "G-type" domains, the dark-CL to "B-type" zones and intermediate luminescence matches the "Y-type" rims (e.g. grains #26 and #27). **d** Examples of altered apatite crystals with cloudy, intermediate to dark CL (grains #22, #37 and #43), transverse cracks (grains #4 and #43) and partly resorbed core (grain #60)
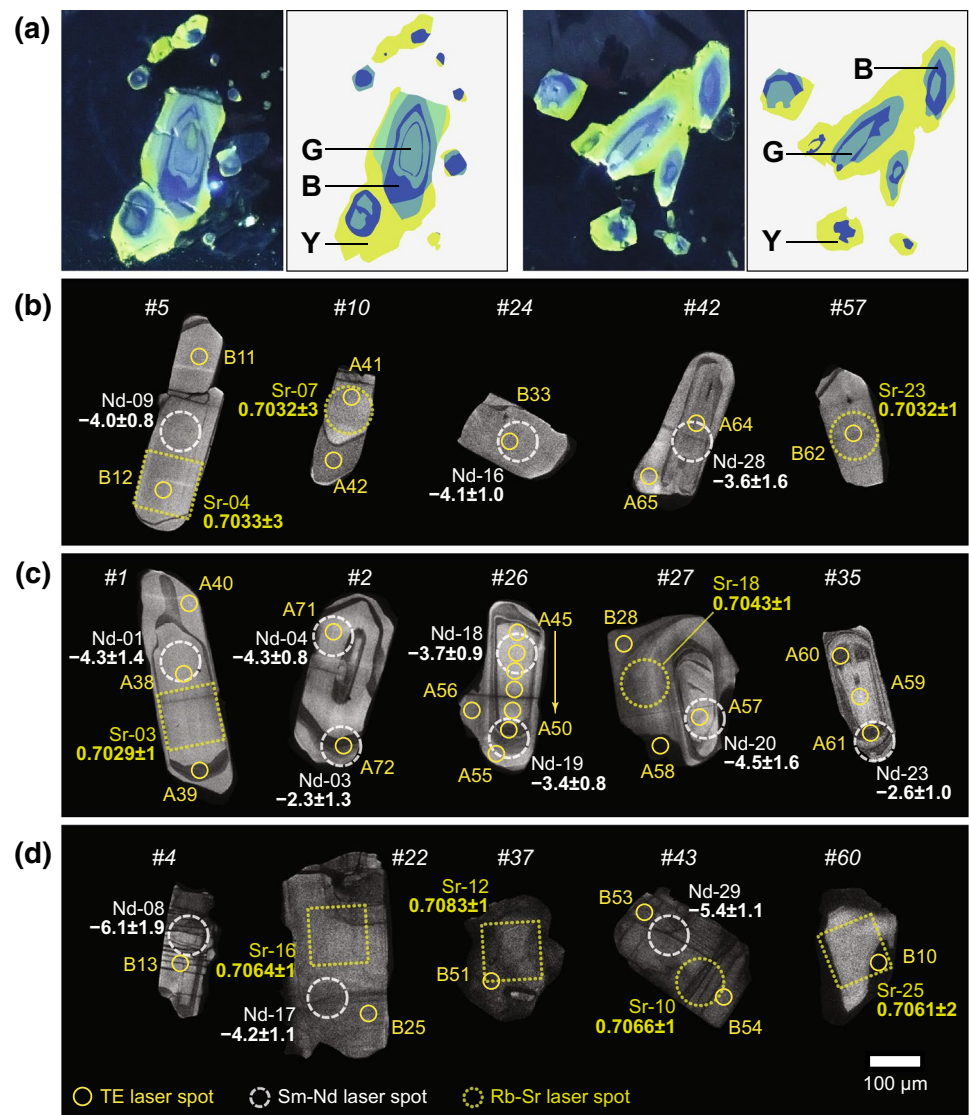

labelled "G"; (2) dark blue luminescence, labelled "B"; and (3) yellowish green luminescence, labelled "Y". SEM-CL images of apatites extracted for chemical and isotopic analyses show the same features, dark grey luminescence being correlated to "B-type" zones and light grey luminescence to "G-type" domains; "Y-type" zones have intermediate luminescence (Figs. 5b–d, 6).

Some of the apatite crystals are characterized by a volumetrically dominant, unzoned G-type core (light grey in SEM-CL images), and a generally very thin (<10 μm) B-type irregular rim (very dark grey in SEM-CL images) (Fig. 5b). Many grains are yet characterized by a sub-oscillatory zoning pattern characterized by the alternation of thin (10–40 μm wide) B- and G-type zones around a homogeneous, G-type core (Figs. 5c, 6). An outermost, unzoned Y-type rim (medium to dark grey in SEM-CL images) may occur and often clearly truncates the B–G zoning (Fig. 5a–c). In some cases, the Y-type domain represents most of the grain volume, or connects individual G–B-zoned crystals with each other (Fig. 5a). Importantly, Y-domains are developed best around apatite crystals that are located at grain boundaries (Fig. 4a–c).

Apatite CL zoning is strongly correlated to trace element concentrations (reported in Supplementary Material; Table S1), especially REE and HFSE, as already described in previous studies (e.g. Kempe and Götze 2002; Dempster et al. 2003; Słaby et al. 2011a) (Fig. 6). The G-type domains show intermediate and relatively homogeneous concentrations in REE (ΣREE = 3000–5000 ppm) relative to the B-type zones that are much richer (ΣREE > 6000 ppm and up to 1.5 wt%, consistent with the activation of bluish CL colours by REE; Kempe and Götze 2002) and to the Y-type rims that show the lowermost concentrations in REE (ΣREE < 3000 ppm and most often between 200 and 1500 ppm) (Fig. 6). Yet, it must be noted that all domains show similar REE ratios, with moderately
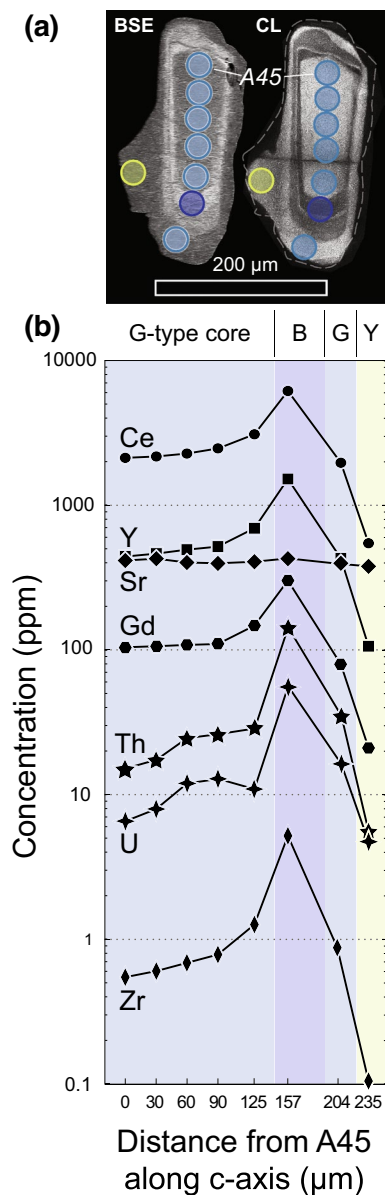
Fig. 6 Representative example of the correlation between textural and chemical characteristics of zoned apatites: **a** BSE and CL images of grain #26 showing the position of the LA-ICP-MS spots for trace element analyses (*colour-coded* as a function of the analysed domain); and **b** corresponding variability of trace element concentrations (*black solid* profiles corresponding to different chemical elements) along the *c*-axis of the grain; the distance is indicated in microns relative to the first spot (A45)

fractionated profiles (La_N/Yb_N = 10–25), high La_N/Sm_N (4–10), a negative Eu anomaly (Eu_N/Eu^* = 0.5–0.8) and a flattish HREE profile (Gd_N/Yb_N = 0.5–1.5). HFSE concentrations are strongly correlated to the REE (Fig. 6): the B-type domains are also very rich in Y (600–1600 ppm), Th (50–150 ppm), U (20–80 ppm) and Zr (1.5–5.0 ppm) compared with the G-type domains (Y = 300–700 ppm; Th = 10–40 ppm; U = 5–20 ppm and Zr = 0.2–1.2 ppm),

whereas the Y-type rims show the lowermost concentrations (generally Y < 500 ppm; Th < 25 ppm; U < 10 ppm and Zr < 0.8 ppm). As a result, many grains show a G-type core having fairly homogeneous REE and HFSE concentrations, surrounded by a B-type zone in which these concentrations increase by a factor 2–5, and by another G-type zone in which REE and HFSE contents are similar to lower than those of the core (Fig. 6). The outermost, Y-type rim shows concentrations that are 2–5 times lower than in the G-type core. Absolute concentrations in each CL domain may vary from a grain to another, but the relative variations between the different domains are systematic.

Regarding the LILE, concentrations in Rb (0.1–1.0 ppm) and Ba (0.05–0.5 ppm) are close to the detection limit. Sr contents are strikingly homogeneous at the scale of the whole apatite population; irrespective of the CL domain, analyses have identical concentrations within uncertainty, ranging from 370 to 430 ± 30 ppm (average 2 SE). Furthermore, all apatites do not show any Sr zoning whatsoever. Even in the crystals that are zoned for REE–HFSE, Sr concentrations are indeed constant across the different domains (Fig. 6). Pb contents vary from 5 to 35 ppm and are positively correlated with REE, ranging from low in the Y-type domains (<10 ppm) to high in the B-type zones (15–35 ppm).

Finally, some apatite grains show clear evidence for alteration (Fig. 5d), such as (1) the presence of cracks perpendicular to the ⟨c⟩ axis, having very dark CL luminescence and cross-cutting the zoning defined above; (2) grains with cloudy and/or irregular, dark-CL luminescence lacking any conspicuous zoning; and (3) dark-CL rims irregularly developed at the expense of homogeneous, bright-CL cores. The trace element geochemistry of these "altered" grains is very similar to that of the Y-type domains, i.e. with typically low concentrations in REE and HFSE.

Titanite textures and trace element composition

Titanite forms large (250–500 μm long and up to 1 mm), prismatic to stubby crystals ranging from subhedral to anhedral (Fig. 4a), sometimes even developing an interstitial habit (Fig. 4c). They are most often associated with biotite + epidote clusters (Fig. 4a), but locally occur in the quartzo-feldspathic matrix (Fig. 4c). Titanite frequently contains inclusions (10–100 μm) of euhedral apatite (Figs. 4a–c, 7).

Representative BSE images of titanites are presented in Fig. 7. Most titanite grains are unzoned/homogeneous. Only a few crystals show either sector or faint, continuous zoning from light to medium grey. Irregular domains with darker BSE than the rest of the crystal occasionally occur along fractures or at grain edges.

All titanite analyses show weakly fractionated REE patterns (La_N/Yb_N = 2–8), but differences in concentration
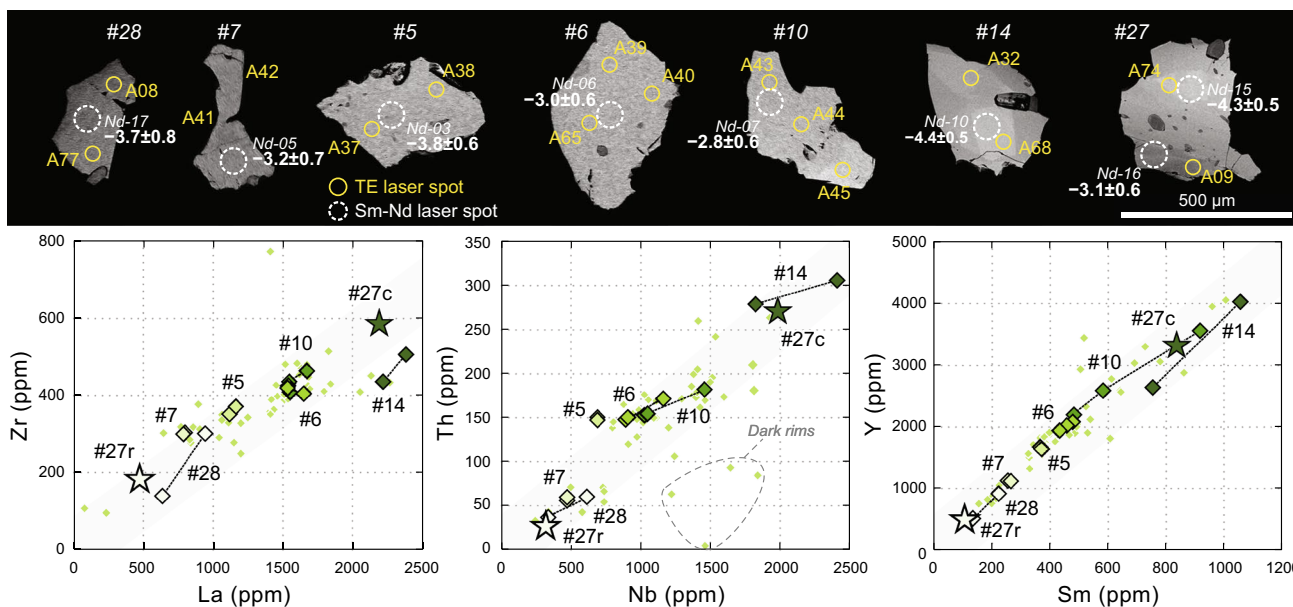
Fig. 7 Representative examples of BSE images of titanite grains from MAT-13 (*top*) and their trace element concentrations in Zr vs. La; Th vs. Nb and Y vs. Sm diagrams (*bottom*). The grains with BSE images reported above are represented by *larger symbols*; and spots analysed from the same grain are represented by the *same colour* and joined by a *dashed line* (with corresponding grain number). An exception is grain #27 from which analyses of core (#27c, *dark green star*) and rim (#27r, *light green star*) are separated
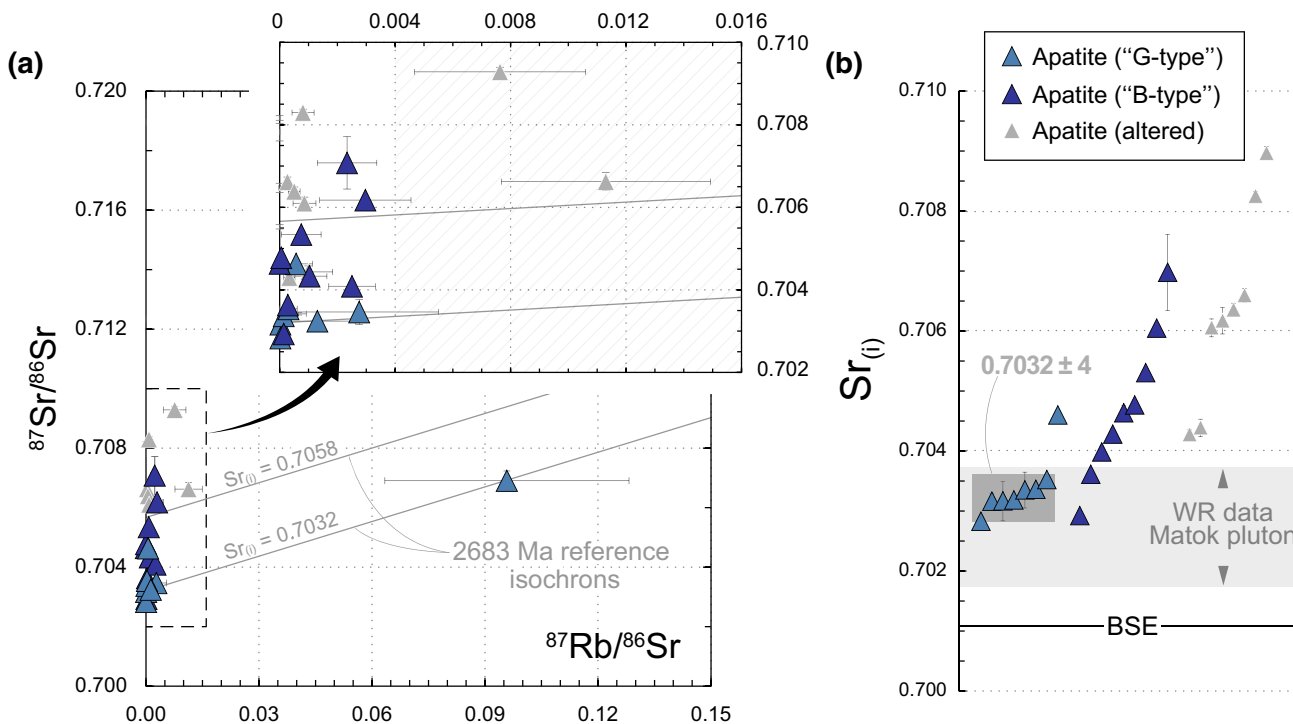
Fig. 8 Results of LA-MC-ICP-MS Rb–Sr isotopic analyses from apatites. **a** "Isochron" diagram of measured $^{87}Sr/^{86}Sr$ vs. $^{87}Rb/^{86}Sr$ ratios. The *hatched domain* corresponds to $^{87}Rb/^{86}Sr > 0.004$ for which age correction on $^{87}Sr/^{86}Sr$ is significant at 2683 Ma. Two reference isochrons at 2683 Ma are reported together with the corresponding initial $^{87}Sr/^{86}Sr$ ($Sr_{(i)}$). **b** 1-D plot of the calculated $Sr_{(i)}$ for individual apatite analyses at 2683 Ma. The light grey field corresponds to the range of Sr(i) measured in whole-rock samples of the Matok pluton (Barton et al. 1992); the BSE value was obtained using the parameters of Workman and Hart (2005). All *error bars* correspond to 2 SE uncertainties

up to one order of magnitude, ΣREE ranging from 0.25 to 2.5 wt% (mostly in the range 1.0–1.75 wt%). Most analyses are characterized by nearly flat to slight convex downwards LREE profiles ($La_N/Nd_N = 0.5$–1.5) and flat HREE profiles ($Gd_N/Yb_N = 1.0$–1.5) together with a negative Eu anomaly ($Eu_N/Eu^* = 0.6$–0.8). Concentrations in HFSE also show important variations, up to one order of magnitude ($Y = 400$–4000 ppm; $Zr = 100$–600 ppm; $Hf = 5$–50 ppm; $Nb = 250$–2500 ppm; $Ta = 10$–600 ppm; $Th = 30$–300 ppm and $U = 20$–80 ppm). Regarding the LILE, Sr contents are homogeneous (ca. 30–50 ppm) whereas Pb contents range from 10 to 90 ppm and are correlated to REE concentrations. The grains contain very minor amounts of Rb (0.1–1.0 ppm) and Ba (ca. 0.1 ppm).

The concentrations of REE and HFSE are positively correlated, as is shown by the nearly linear trends in Fig. 7. In contrast to apatite, the chemical variability of titanite is mostly reflected by inter-grain compositional differences, rather than intra-grain zoning (Fig. 7). Indeed, the systematic analysis of several spots within individual crystals reveals that most titanite grains are compositionally homogeneous, except the few crystals showing sector zoning (Fig. 7). A single crystal (#27) shows nearly the entire compositional range (estimated on all other grains) between its REE- and HFSE-rich core (bright in BSE) and REE- and HFSE-poor rim (dark in BSE) (Fig. 7).

Rb–Sr isotopes

The results of Rb–Sr isotopic analyses of apatite are reported in Supplementary Material (Table S2) and presented in Fig. 8. Because of the large laser spot sizes used for apatite (90–180 µm), the small-scale zoning in many grains could not be resolved, and obtained initial Sr isotope ratio may result from the analysis of more than one zone. The results in Fig. 8 are, therefore, reported according to the predominant zone sampled by the laser, i.e. G-, B-type or altered grains/domains.

Most apatite grains have $^{87}Rb/^{86}Sr$ ratios below 0.004 (Fig. 8a), making any age correction (at 2683 Ma) insignificant, i.e. initial $^{87}Sr/^{86}Sr$ ratios (reported hereafter as $Sr_{(i)}$) are identical within uncertainty to the measured ones (Table S2). The G-type apatites show relatively homogeneous $Sr_{(i)}$, the majority of the analyses being identical within uncertainty and range from 0.7028 to 0.7046 (Fig. 8b). Excluding the one outlier with the highest value, G-type apatites yield an average $Sr_{(i)}$ of 0.7032 ± 4 (2 SD; $n = 7$), which notably falls within the range of $Sr_{(i)}$ measured on whole-rock samples from the Matok pluton (0.7018–0.7038; Barton et al. 1992). The B-type and altered apatites show a much wider scatter in $Sr_{(i)}$, ranging from 0.7029 to 0.7070, and 0.7043 to 0.7090, respectively (Fig. 8b). All values correspond to more radiogenic isotope composition than the

Bulk Silicate Earth at that time (0.7011; calculated using the parameters of Workman and Hart 2005).

Sm–Nd isotopes

The results of Sm–Nd isotopic analyses of apatite and titanite are reported in Supplementary Material (Table S3) and presented in Fig. 9. The spot sizes of 75 µm used for apatite analyses precluded a proper analysis of individual growth zones, in particular of the G- and B-types. The data from apatites are thus sorted according to the crystal domain representing the largest volume during analysis, i.e. G-, B-type or altered (Fig. 9).

The G- and B-type apatite analyses have a similar and relatively restricted range of Sm–Nd isotopic compositions, with $^{147}Sm/^{144}Nd$ ratios in the range 0.0733–0.0936 and $^{143}Nd/^{144}Nd$ ratios between 0.51028 ± 11 and 0.51065 ± 15 (Fig. 9a). In contrast, altered apatite grains/domains show a greater spread in $^{147}Sm/^{144}Nd$ (0.0727–0.1177) and $^{143}Nd/^{144}Nd$ (0.51002–0.51102) ratios (Fig. 9a). Titanites are characterized by higher $^{147}Sm/^{144}Nd$ (0.0914–0.1386) and $^{143}Nd/^{144}Nd$ (0.51067–0.51142) than most apatite grains (Fig. 9a). Altogether, the G-, B-type apatites and titanites define an isochron that corresponds to an age of 2713 ± 130 Ma (MSWD = 2.5; $n = 39$) (Fig. 9a), whereas the altered apatite grains plot clearly off this isochron. Although imprecise, the Sm–Nd isochron age is very close to, and within uncertainties of the emplacement age of the Matok pluton suite (2683 Ma). The whole-rock sample MAT-13 (Laurent et al. 2014c) also plots on this isochron (Fig. 9a).

All calculated $\varepsilon Nd_{2683\ Ma}$ correspond to subchondritic values (Fig. 9b). All G- and B-type apatites have $\varepsilon Nd_{2683\ Ma}$ that overlap within uncertainty and are comprised between -4.5 ± 1.6 and -2.3 ± 1.3. A nearly identical range (from -4.6 ± 0.6 to -2.6 ± 0.6) was also obtained from the titanites grains; as the uncertainties for titanite analyses are smaller, there are significant differences in $\varepsilon Nd_{2683\ Ma}$ between grains/domains (Fig. 9b, see also Fig. 7). Importantly, the range in $\varepsilon Nd_{2683\ Ma}$ values obtained from apatite (G, B-types) and titanite is significantly wider compared to the value obtained by the whole-rock analysis (-2.8 ± 0.7; Laurent et al. 2014c). The altered apatites show an even much wider range in $\varepsilon Nd_{2683\ Ma}$ values from -8.3 ± 1.9 to -2.4 ± 1.8 (Fig. 9b).

Discussion

Accessory mineral saturation

Apatite is an early crystallized phase, as it forms euhedral crystal inclusions in every other mineral of the rock, including titanite (Figs. 4, 7). Consistently, the apatite saturation
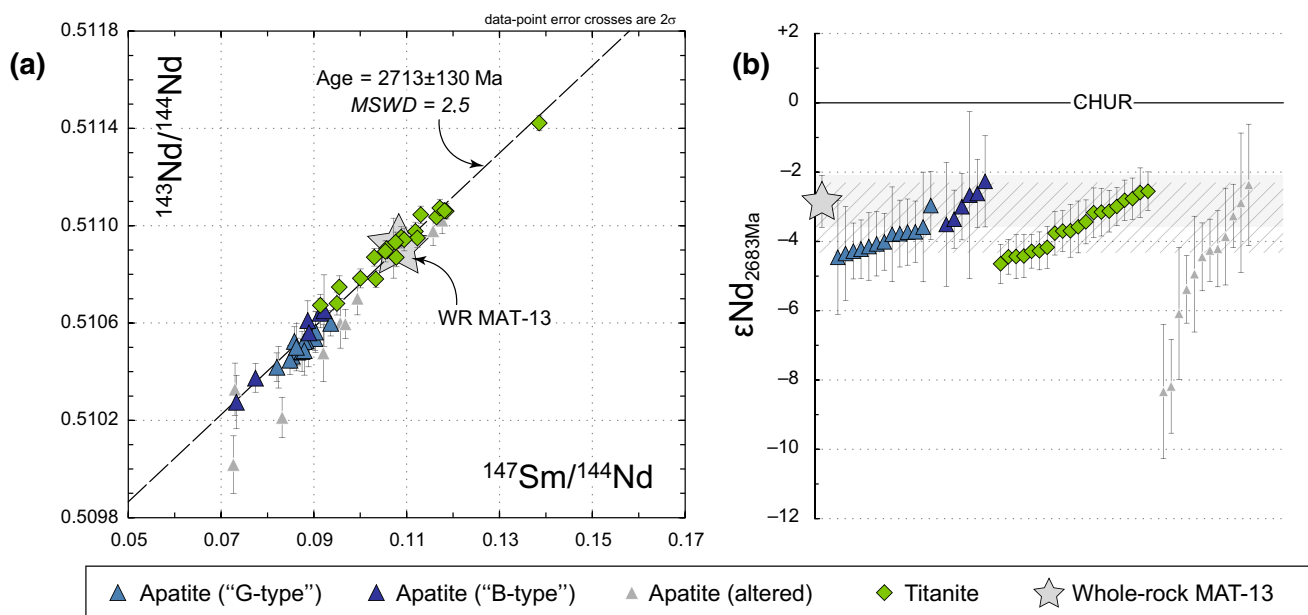
Fig. 9 Results of LA-MC-ICP-MS Sm–Nd isotopic analyses from apatites and titanites. **a** "Isochron" diagram of measured $^{143}Nd/^{144}Nd$ vs. $^{147}Sm/^{144}Nd$ ratios. The *dashed line* represents the isochron calculated using analyses from titanites, G- and B-type apatites. The *star* corresponds to the composition of the bulk-rock sample MAT-13 (Laurent et al. 2014c). **b** 1-D plot of the calculated εNd_t for individual apatite and titanite analyses at 2683 Ma. The *grey field* corresponds to the composition of the whole-rock ($\varepsilon Nd_t = -2.7 \pm 0.7$; Laurent et al. 2014c) while the hatched field corresponds to the average $\pm$ 2 SD of all Matok whole-rock samples (Fig. 2c). The CHUR model is from Jacobsen and Wasserburg (1984). All error bars correspond to 2 SE uncertainties

temperature of sample MAT-13 (calculated using the geo-thermometer of Harrison and Watson (1984)) is 1023 °C, which is consistent with experimental constraints on compositions close to those of the Matok granitoids showing that apatite is typically a liquidus phase formed at 1000–1050 °C (Bogaerts et al. 2006).

Titanite contains abundant inclusions of apatite (Figs. 4, 7), indicating that it crystallized later. Moreover, the crystals range from euhedral to anhedral (Fig. 7), suggesting that they formed at higher crystal fraction than apatite. This is supported by the temperatures of titanite crystallization in MAT-13 (calculated using the Zr-in-sphene thermometer of Hayden et al. 2008; see details in Table S1), ranging from 776 to 915 °C (±26 °C), with an average of 860 ± 46 °C (2 SD, $n = 66$). This temperature is consistent with the fact that titanite formed slightly earlier than, or coeval with biotite and epidote (Fig. 4) that are expected to crystallize in the temperature interval 850–750 °C, as shown by experimental phase relationships in metaluminous granitoid systems (Johnston and Wyllie 1988; Schmidt and Thompson 1996; Bogaerts et al. 2006).

Origin of chemical variations in apatite

It is pertinent to note that all apatite grains/domains in sample MAT-13 show similar Sr concentrations (396 ± 39 ppm;

2 SD, $n = 88$), but large variations (and systematic zoning) in REE and Y contents (Fig. 6). Both observations hint that the Sr content of apatite was re-equilibrated by intra- and inter-grain diffusion, but not the REE and Y contents. Therefore, Sr contents will not be considered further for the interpretation of primary magmatic zoning in apatite.

Many apatite grains show an abrupt increase of REE and HFSE concentrations from G-type core to B-type rim by a factor 2–5 (Fig. 6). This variation is inconsistent with Rayleigh fractionation, as this process would result in (1) a decrease of REE and Y contents from core to rim (Bruand et al. 2014); and (2) a negative correlation between apatite-compatible elements (REE, Y) and apatite-incompatible elements (Zr, Nb, Ta), which is opposite to the observed trend (Fig. 6). Kinetic effects, such as the formation of a chemical boundary layer due to high apatite growth rate (Bacon 1989), can also be ruled out, as this would also result in a negative correlation between apatite-compatible and apatite-incompatible elements (Tepper and Kuehner 1999). Hence, the observed concentric zoning most likely results from abrupt changes of the melt composition during apatite crystallization (Tepper and Kuehner 1999; Słaby et al. 2011a; Bruand et al. 2014) and, therefore, records the magma mixing process.

The much lower trace element concentrations in Y-type relative to G- and B-type domains (Fig. 6) might

be explained either by Rayleigh fractionation or kinetic effects, e.g. during late apatite growth from isolated melt pockets in a highly crystallized mush (Dempster et al. 2003). However, the observation that both apatite-compatible (REE, Y, Th, U) and apatite-incompatible elements (Zr, Nb, Hf, Ta) are depleted in the Y-type domains (Fig. 6) rules out these processes. Instead, we suggest that the Y-type rims (re)crystallized from interstitial fluids. This conclusion is supported by the similar composition between the Y-type rims and the altered apatite grains/ domains; and the fact that the Y-type rims are best developed around apatite grains located along grain boundaries (Fig. 4) and often cross-cut the G–B-type zoning (Figs. 4, 5). Moreover, such textures and CL colours (especially the yellowish luminescence activated by the presence of Mn^{2+} in the crystal structure) are typical of apatite formed by fluid-induced (re)crystallization or alteration in igneous rocks, pegmatites and mineralized veins (Hodson and Finch 1997; Kempe and Götze 2002; Słaby et al. 2011a). The percolation of late fluids in MAT-13 is further supported by CL images of plagioclase and K-feldspar crystals, showing a reduced luminescence at their margins (Fig. 4): this commonly results from a decrease of the defect density in fluid-recrystallized domains (Graham and Elphick 1990; Kronenberg et al. 1996).

Our interpretations of the origin of chemical zoning in apatite are supported by results of Polytopic Vector Analysis (PVA) that are described in detail in the Supplementary Material and summarized in Fig. 10. PVA indicates that the chemical variability of apatites in MAT-13 can indeed be explained by various contributions of three end-member compositions EM1, EM2 and EM3, which compositions, respectively, correspond to (1) a REE-rich apatite with fractionated REE patterns; (2) an apatite poor in all trace elements, except Na; and (3) a moderately REE-rich apatite with negative Eu anomalies and strong Y enrichment relative to the REE. EM1 and EM3 are both consistent with compositions of igneous apatites, but crystallized from chemically distinct magmas; whereas the low trace element contents and Na enrichment of EM2 are very typical of hydrothermal apatites (Zirner et al. 2015). Consistently, G- and B-type domains have low proportions of the EM2 end-member (<15%) relative to the Y-type and altered apatites (up to 95%) (Fig. 10), supporting that the latter are fluid-derived. G- and B-type apatites do not show strongly different end-member proportions because the compositional scatter of the Y-type and altered grains control the chemical variability of the dataset (see Supplementary Material for details). Nonetheless, B-type domains show greater affinities to EM3 (25–40 and up to 50%) than G-type domains (10–30%) (Fig. 10), supporting that the two types crystallized from two, compositionally distinct silicate melts.
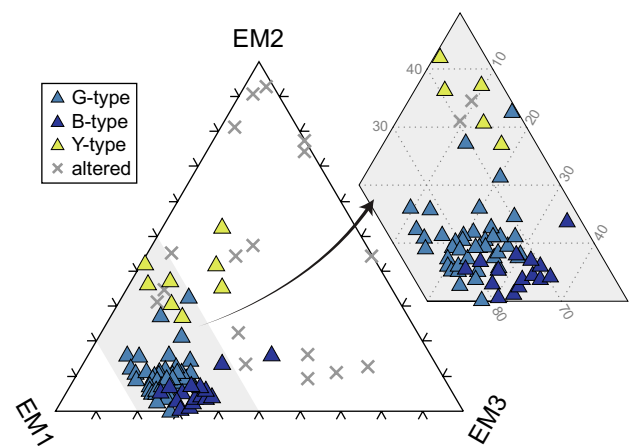
Fig. 10 Results of Polytopic Vector Analysis (PVA) summarized in a ternary diagram showing the relative proportions of the three modelled end-members (EM1, EM2 and EM3) for each apatite trace element analysis. EM1 and EM3 are interpreted as igneous apatite compositions, respectively, LREE-rich with fractionated REE pattern and REE-Y-rich with less fractionated REE pattern and negative Eu anomaly; EM2 corresponds to an apatite poor in all trace elements, except Na and Sr. Details about the model and results are reported in the Supplementary Material

Origin of chemical variations in titanite

Disequilibrium uptake of trace elements in titanite has been previously documented (Bruand et al. 2014; McLeod et al. 2011) and results from high crystal growth rates relative to lattice diffusivity (Watson and Liang 1995). However, this effect is negligible here, as such disequilibrium conditions result in (1) extreme HFSE contents (e.g. Nb = 2000–3500 ppm; Bruand et al. 2014), typically an order of magnitude higher than in MAT-13 titanites (Nb = 300–500 ppm); and (2) unrealistically high Zr-in-sphene temperatures (>1000 °C; Hayden et al. 2008), while those we obtained are in good agreement with petrography and the saturation temperatures of other minerals (see above).

Besides a few grains that exhibit a clear sector zoning and significant intra-grain chemical variations (e.g., grain #27), most titanites lack any zoning and display huge inter-grain compositional differences (Fig. 7). This feature cannot be the result of diffusion because self-diffusion for most elements in titanite is similar to apatite, for instance for the REE (e.g. D^{Nd} of ca. 10^{-20} m^2 s^{-1} at 1000 °C; Cherniak 1995, 2000), and titanite crystallized at temperatures ca. 150 °C lower than apatite. The enormous inter-grain chemical variation in titanites could be interpreted either by: (1) successive formation of titanite grains at different stages of a Rayleigh fractionation process, or (2) the simultaneous crystallization of titanites from melt domains having distinct characteristics, such as degree of melt polymerization (Green and Pearson

1986; Prowatke and Klemme 2006a; Sawka et al. 1984), aluminium saturation index (Prowatke and Klemme 2005) or volatile contents (Sawka et al. 1984; Tiepolo et al. 2002) that all affect element partitioning in titanite.

The fact that one titanite grain shows a clear decrease of trace element concentrations from core to rim (e.g. grain #27; Fig. 7) favours the first hypothesis. Moreover, the titanites with the lowest contents in HFSE and REE often show anhedral crystal shapes (Fig. 7) suggesting that they formed late in the crystallization history, in melt pockets depleted in these elements during previous titanite crystallization. Nevertheless, the titanite analyses define nearly linear arrays in the binary diagrams of Fig. 7, which is at odds with pure Rayleigh fractionation that would result in curved trends, especially since the considered elements have different affinities with titanite ($Kd_{Nb}^{Ttn/L} > Kd_{Th}^{Ttn/L}$; $Kd_{La}^{Ttn/L} > Kd_{Zr}^{Ttn/L}$; $Kd_{Sm}^{Ttn/L} \sim Kd_{Y}^{Ttn/L}$; Green and Pearson 1986; Prowatke and Klemme 2005; Tiepolo et al. 2002). These linear arrays rather point to crystallization from two distinct melt domains, as a result of magma mixing (McLeod et al. 2011). We, therefore, interpret the compositional variability of the entire titanite population in sample MAT-13 as reflecting the crystallization from a mixture of two magmas, accompanied by Rayleigh fractionation in local melt patches. The involvement of compositionally different magmas is also supported by the significant variations in εNd_t, not only in different titanite grains (from ca. −5 up to −2; Fig. 9b), but also within a single crystal (grain #27; Fig. 7).

Chemical and isotopic characteristics of the mixed magmatic end-members

Hereafter we discuss the origin of the two magmatic end-members based on the chemical-isotopic composition of apatite and titanite, modelling of mineral-melt partitioning, and PVA results.

The composition of apatite strongly depends on the chemistry of its host magma (Belousova et al. 2001; Chu et al. 2009; Miles et al. 2013; Sha and Chappell 1999; Jennings et al. 2011). A compilation of data shows that apatite in "S-type", peraluminous and purely crust-derived granites contain higher Y, lower Ce contents and lower Th/U and La/Sm ratios than apatite crystallized from "I-type", metaluminous and ultimately mantle-derived granitoid suites (Fig. 11a). All apatite analyses from sample MAT-13, irrespective of the domain (G-, B-, Y-type or altered grains), have high Ce/Y, Th/U and La/Sm ratios matching the compositional field of apatite in "mantle-derived" granitoids (Fig. 11a). The composition of the Matok apatites is, moreover, very different from that of apatite in TTGs or biotite granites from the PB (O. Laurent, unpublished data) (Fig. 11a). This difference precludes that the felsic end-member was similar in composition to either

TTGs or biotite granites. Alternatively, the very similar element ratios of all apatite domains in sample MAT-13 (Figs. 6, 11a) more likely reflect interaction of two cogenetic magmas at different stages of differentiation from mantle-derived melts, i.e. a "self-mixing" process (e.g. Alves et al. 2009; Couch et al. 2001; Pin et al. 1990; Wiebe et al. 2007).

A compilation of apatite/melt partition coefficients for relevant compositions (Fujimaki 1986; Luhr et al. 1984; Prowatke and Klemme 2006b; Nagasawa 1970; Nagasawa and Schnetzler 1971; Watson and Green 1981) shows that partitioning of REE and HFSE in apatite typically increases with the silica content of the melt (see Supplementary Material, Fig. SM1). Based on a parametrization of $Kd_i^{Ap/L}$ values as a function of melt SiO_2 content for the best-documented elements (La, Ce, Sm, Gd, Dy and Y; Fig. SM1), we calculated the hypothetical composition of apatites crystallized from whole-rock samples of the Matok suite (approximating them as liquids). The results show that the higher the SiO_2 content of the melt, the higher the calculated Y and REE content of apatite (Fig. 11b). This co-variation is not an artefact inherited from whole-rock compositions because there is no correlation whatsoever between Y and REE contents of whole rock samples in the Matok suite (Fig. 11b). Based on these results, the Y and REE contents of G-type apatite cores match those of apatite crystallized from melts having <60 wt% SiO_2 (Fig. 11b), typical for the Matok diorites (Fig. 2). In contrast, the higher Y and REE contents of the B-type domains are consistent with crystallization from melts having up to 65–70 wt% SiO_2 (Fig. 11b), i.e. similar to the Matok's most felsic granodiorites (Fig. 2).

The PVA results (see Fig. 10 and Supplementary Material) support these interpretations. Although they partly overlap (see discussion above and Supplementary Material), G- and B-type apatite domains are distinguished by different proportions of the EM1 and EM3 end-members (70–85 and 10–30% for G-type; 60–80 and 25–35% for B-type; Fig. 10), interpreted as reflecting apatite crystallized from two distinct silicate melts (see above). B-type domains are characterized by greater proportions of EM3, i.e. an apatite richer in HREE and Y than EM1, in agreement with the partitioning model (Fig. 11b) and pointing to crystallization from a felsic melt (Belousova et al. 2001; Chu et al. 2009). EM3 apatite also has a stronger negative Eu anomaly than EM1 (see Supplementary Material), suggesting that the melt from which it crystallized underwent plagioclase fractionation. This supports the interpretation that such melt would be a differentiated product of the Matok diorites since the evolution thereof involves significant plagioclase fractionation (Laurent et al. 2014c). In turn, EM1 shows lesser REE-Y contents and more fractionated REE patterns than EM3, which is very typical of apatites crystallized from mafic magmas (Belousova et al. 2001; Chu et al. 2009; Miles et al. 2013).

Fig. 11 Constraints on the nature of the two mixed magmas based on ▶ apatite chemistry. **a** Plots of Y vs. Ce concentrations (*top*) and Th/U vs. La/Sm ratios (*bottom*) in which the apatite analyses from MAT-13 are compared to apatite analyses from "S-type", strongly peraluminous, crust-derived granites (*orange symbols and fields*), "I-type", metaluminous to slightly peraluminous, mantle-derived granitoids (*purple symbols and fields*) (data from Belousova et al. 2001; Bruand et al. 2014; Chu et al. 2009; Miles et al. 2013); and apatite analyses from TTGs and biotite-bearing granites of the PB (O. Laurent, unpublished data). Note that the latter match the composition of apatites from crust-derived granites, whereas all apatite domains from MAT-13 have the same compositions as those from "mantle-derived" granitoids. **b** Plot of Y vs. REE (La + Ce + Sm + Gd + Dy) concentrations in apatites from MAT-13 compared to virtual apatite compositions (*reddish circles and fields*) calculated from the SiO_2 content of Matok bulk-rock samples (indicated in the caption) and Kd values from the SiO_2-dependent parameterization presented in Supplementary Material (Fig. S1). Note that the higher the SiO_2 content of the rock, the higher the modelled Y and REE content of virtual apatite compositions. The *inset* shows the composition of whole-rock samples of the Matok pluton (symbols as in Fig. 2; data from Laurent et al. 2014c) showing that there is no particular correlation between Y and REE concentrations

Interestingly, the composition of the titanite grains/domains showing the highest REE, HFSE contents and lowest Nb/Ta ratios in sample MAT-13 is very close to a composition calculated for titanite crystallized from a melt similar to the Matok diorites (using partition coefficients from Prowatke and Klemme 2005; Fig. 12). These compositions correspond to subhedral crystals or the cores of zoned grains (Fig. 7), suggesting that these grains/domains crystallized early from the dioritic magma. These early titanite grains/domains also show the lowest $\varepsilon Nd_{2683\ Ma}$ of ca. −4.5 (Fig. 12), probably reflecting the isotopic composition of the dioritic magma. The other titanite grains/domains showing similarly low $\varepsilon Nd_{2683\ Ma}$ of ca. −4.5, but lower REE, HFSE contents and higher Nb/Ta, would have formed from dioritic melt after some extent of Rayleigh fractionation (Fig. 12). On the other hand, there are titanite grains showing (1) significantly higher εNd_t up to ca. −2.5, and (2) lower REE, HFSE contents and higher Nb/Ta ratios than the grains crystallized from the dioritic melt (Fig. 12). Furthermore, rare crystals have a REE-, HFSE-rich core with low $\varepsilon Nd_{2683\ Ma}$ surrounded by a REE- and HFSE-poor rim with significantly higher $\varepsilon Nd_{2683\ Ma}$ (see grain #27; Fig. 7). These characteristics require a combination of Rayleigh fractionation and involvement of a melt having more radiogenic Nd isotopic composition, lower trace elements and higher Nb/Ta (Fig. 12). This points to mixing with a more felsic magma, having already undergone crystallization of titanite ± hornblende (that also preferably scavenges Y as well as Ta relative to Nb).
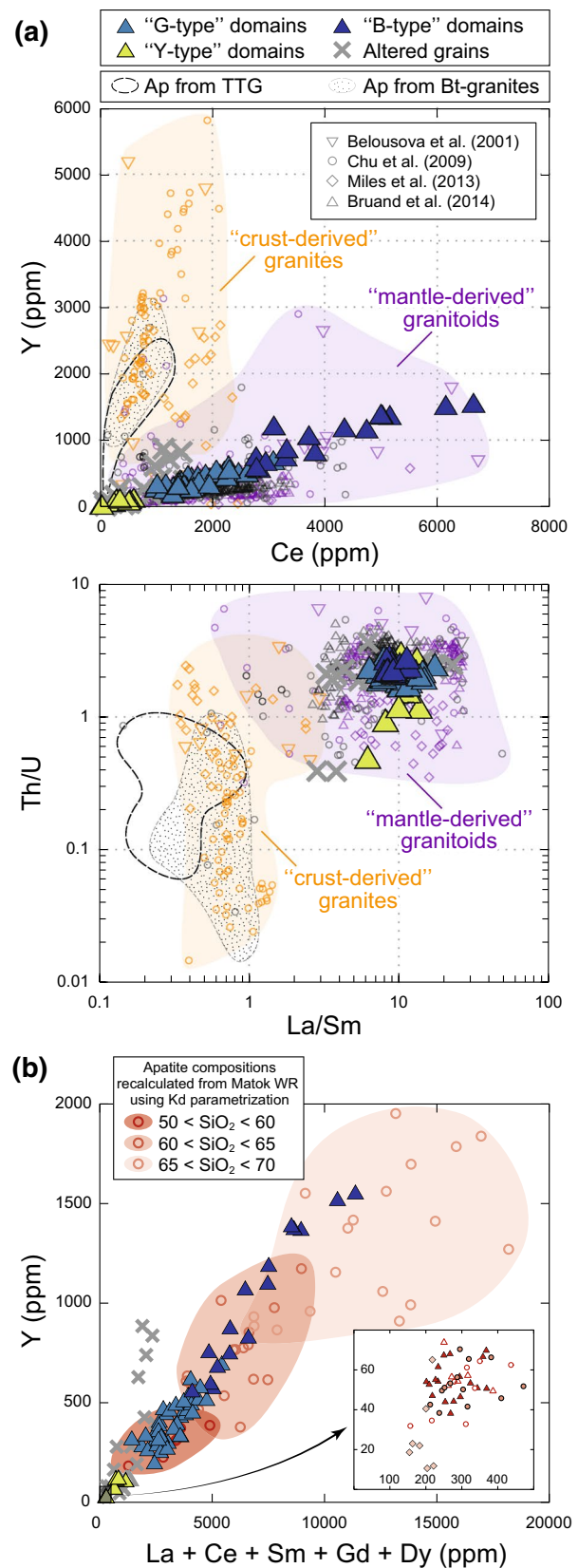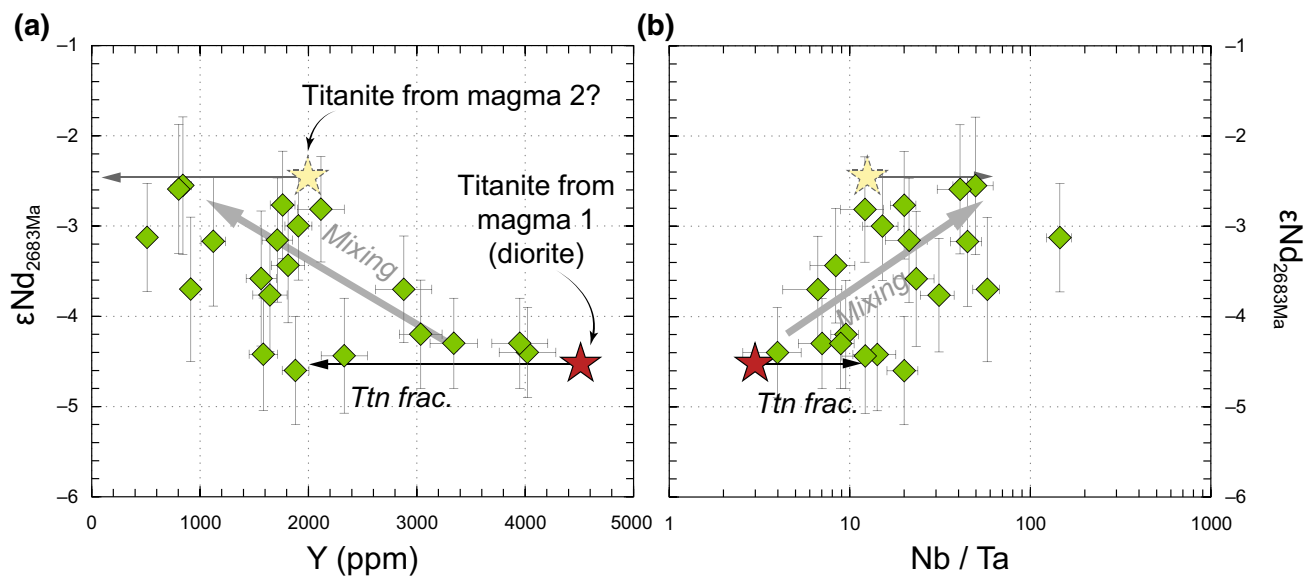
Fig. 12 Plot of εNd_t of titanite grains in sample MAT-13 (*green diamonds*) as a function of **a** Y concentrations (in ppm) and **b** Nb/ Ta ratios analysed from the same crystal domains. The *red star* represents the virtual composition of titanites from a melt with $\varepsilon Nd_t = -4.5$ and having the same trace element composition as diorites from the Matok pluton (calculated using the average composition of diorites and partition coefficients from Prowatke and Klemme 2005—average of data for melts with aluminium saturation index >0.5). The *black arrow* represents the effect of 1 wt% titanite frac-

tionation on Y concentrations and Nb/Ta ratios, calculated using partition coefficients from Prowatke and Klemme 2005 (same as above). The *dashed yellow star* represents the putative composition of titanites crystallized from a more felsic melt (having lower Y and higher Nb/Ta owing to 1 wt% titanite fractionation) with $\varepsilon Nd_t = -2.5$. The *light grey arrow* qualitatively represents the compositional range of titanites from melts resulting from various extent of titanite fractionation and mixing between the two putative melt end-members. All *error bars* correspond to 2 SE uncertainties

The isotopic variations are more difficult to interpret in the case of apatites because of greater uncertainties and poorer spatial resolution (Fig. 5). However, the range of $\varepsilon Nd_{2683\ Ma}$ in G- and B-type apatite domains overlaps that of titanites (Fig. 9) and it is clear that the apatite analyses dominantly from B-type domains systematically have higher εNd_t than those from G-type cores and homogeneous grains (e.g. grains #2, #26 and #35; Figs. 5, 9), which is in line with the observations based on titanites. Moreover, the $Sr_{(i)}$ of the G-type cores and homogeneous grains cluster at about 0.703, whereas it is more scattered and shifted towards higher values (up to 0.707) for B-type domains (Figs. 5, 8).

In summary, the isotopic and trace element characteristics of MAT-13 apatites and titanites hint that the two magmas involved in the "hybridization" zone of the Matok pluton were:

1. a mafic/intermediate magma with εNd_t of ca. −4.5 and $Sr_{(i)}$ of ca. 0.703, similar in composition to the common diorites of the Matok pluton and, like them, formed by limited differentiation of a mafic mantle-derived melt (Laurent et al. 2014c); and

2. a more felsic magma with εNd_t of ca. −2.5 and $Sr_{(i)}$ of ca. 0.707, close in composition to the most felsic Matok granodiorites and likely derived from extensive differentiation of mafic melt similar to the Matok diorites.

Laurent et al. (2014c) and Laurent and Zeh (2015) proposed that the Matok parental mafic magmas stem from a mantle source enriched by the subduction of sedimentary rocks. Various proportions or nature of such sediments could explain the observed differences in Sr–Nd isotopic compositions. In the PB, greywackes and arkoses are characterized by lower $^{147}Sm/^{144}Nd$ and $^{87}Rb/^{86}Sr$ ratios (0.09–0.10 and 0.1–1.4, respectively) than shales (0.10–0.15 and 1.3–30, respectively) (Kreissig et al. 2000). As a result, the source of the dioritic magma would have dominantly been enriched by feldspar-rich sediments, whereas the granodioritic one derives from the differentiation of a melt from a source mainly enriched by shales.

These results have two important implications. First, they support the view that mixing does not necessarily involve magmas from contrasted (i.e. mantle and crustal) sources and can occur between co-genetic magmas. The chemical trends defined by whole-rock samples, such as those defined by the Matok suite (Fig. 2), could thus reflect a combination of fractionation from a common mafic, mantle-derived parent and "self-mixing" between magmas at various stages of the differentiation process, owing to the incremental emplacement and interactions of different magma batches over time (e.g. Glazner et al. 2004) or convective instabilities within a larger magma chamber periodically replenished by mafic magma (e.g. Alves et al. 2009; Couch et al. 2001; Holness et al. 2005).

Second, despite being co-genetic, the two mixed magmas can have different isotopic composition, reflecting an isotopically inhomogeneous source. Although well recorded by the significant isotopic variability of titanites and apatites from MAT-13, such isotopic inhomogeneity is not resolved by bulk-rock isotopic measurements in the case of the Matok pluton. All samples of the suite indeed show identical Sr (Fig. 8) and Nd (Figs. 2 and 9) isotopic compositions within uncertainty. This is because the bulk-rock dissolution artificially homogenizes any mineral-scale variations of the radiogenic and father/daughter isotopic ratios.

Conditions of magma interaction

The complete hybridization between two compositionally different magmas requires the mechanical stirring of heterogeneities to length scales small enough to be rapidly erased by chemical diffusion (e.g. Ottino 1989; Perugini and Poli 2004, 2012; Perugini et al. 2002; Petrelli et al. 2006), i.e. typically less than a few millimeters (Petrelli et al. 2011). This requires a small viscosity contrast between the two magmas (Jellinek and Kerr 1999; Sparks and Marshall 1986; Oldenburg et al. 1989; Poli et al. 1996), which is difficult to fulfil, especially in the case of contrasted end-member compositions (i.e. mafic vs. felsic magmas) because they would have very different crystal fractions at one given temperature (Laumonier et al. 2014a, b).

We have estimated the viscosities of the two mixed magmas in Matok (diorite vs. granodiorite/granite) based on experimental constraints (data from Bogaerts et al. 2006; see details of the calculations in Supplementary Material). The results are presented in Fig. 13a. The two magmas would typically have had a low-viscosity contrast (less than one order of magnitude) down to a temperature of ca. 850 °C; below this threshold, the viscosity contrast rapidly increases, up to 4 orders of magnitude at 775 °C (Fig. 13a). The magma interaction and hybridization, as observed in the field (Fig. 3) and recorded by accessory minerals, therefore, implies that the temperature at which the two magmas were equilibrated in contact with each other was >850 °C, otherwise the diorite would have behaved as a solid phase (>50 wt% crystals; Fig. 13a) and rather formed enclaves in the felsic magma.

Further temperature constraints can be placed using the textural and chemical data from accessory minerals. Internal chemical variations in apatite grains record abrupt changes in the environment of crystallization (Figs. 5, 11), i.e. initial formation from the mafic magma (G-type cores), and subsequent crystallization from the more felsic melt (B-type zones) during the mixing process. This most likely took place by migration of apatite grains from a melt domain to another in the course of crystallization (Perugini et al.
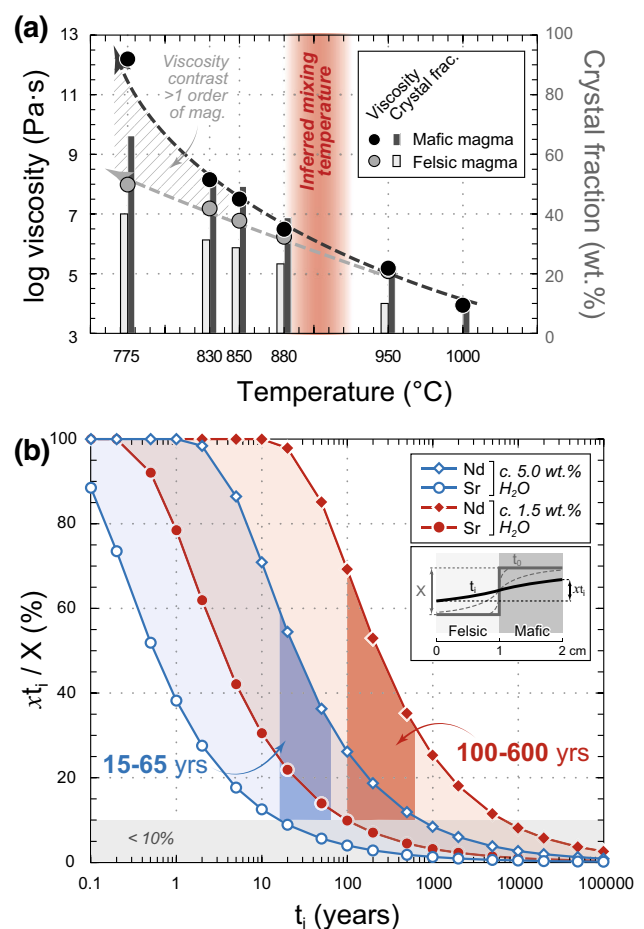
Fig. 13 **a** Results of the rheology model, presented as the absolute viscosity of the two magmas (melt + crystals) and their crystal fraction (in wt.%) as a function of temperature. Phase proportions and liquid compositions are from experimental run products of Bogaerts et al. (2006); viscosities were calculated based on these parameters, using the equations of Giordano et al. (2008) and Costa et al. (2009) (see details in the Supplementary Material). The *vertical red field* highlights the temperature of mixing inferred from petrography and accessory mineral saturation (see text). **b** Results of the diffusive fractionation model used to characterize the duration of chemical hybridization between the liquid phases of the two mixed magmas. The *inset* illustrates a contact zone between a felsic melt (*light grey*) and a mafic melt (*dark grey*); the *solid grey line* represents the initial, absolute concentration gradient (X). The *black solid curve* represents the concentration profile at time t_i, after some extent of chemical diffusion between the two liquids and at which the absolute concentration contrast is represented by xt_i. We consider that diffusion is symmetrical relative to the interface. The extent of chemical equilibration is evaluated using the parameter xt_i/X, which is independent of the initial concentrations. The diagram shows the values of xt_i/X (in %) at different times t_i (in years) for Sr (*circles*) and Nd (*diamonds*) and two melt compositions (water rich and water poor; see text for details), obtained using the diffusion equations of Crank (1975) and at a temperature of 900 °C. The *grey field* corresponds to less than 10% difference between xt_i and X (insignificant regarding analytical uncertainties). The *blue* and *red domains* correspond to the time required to homogenize the Sr concentration gradient to $xt_i/X < 10\%$ while keeping the Nd concentration gradient to $xt_i/X > 33\%$ (see text for details)

2003), as proposed to explain similar zoning in K-feldspar phenocrysts (Słaby et al. 2008, 2010, 2011b). In contrast, the limited intra-grain but large inter-grain chemical variations of the titanite population (Fig. 7) implies crystallization from internally homogeneous melt pockets of a crystal mush, yet having different compositions from one another owing to various extents of magma hybridization and Rayleigh fractionation (Fig. 12). Titanite crystallization thus took place after significant chemical exchanges between the two magmas and cooling, so that the crystal fraction was high enough to isolate individual melt pockets (ca. 30–50% at the temperatures of titanite crystallization, i.e. 820–900 °C; Fig. 13a).

Therefore, the conditions of thermal equilibration between the two magmas must be comprised between the highest Zr-in-sphene crystallization temperatures (ca. 880–900 °C) and that of apatite crystallization in the dioritic melt, i.e. 925–975 °C given that apatite forms within 60–100 °C of the apatite saturation temperature (Piccoli and Candela 1994) (1023 °C in the case of MAT-13). A temperature of ca. 900 °C seems reasonable, especially considering the close rheology of the two magmas (both characterized by viscosities of ca. 1×10^6 Pa s) and low crystal fractions (<30%) at this temperature (Fig. 13a), which would have fostered mechanical stirring and transfer of apatite crystals from a melt domain to another.

Extent and timescales of chemical hybridization

Magma mixing is typically a fractal process (Perugini and Poli 2001), meaning that even in apparently well-mixed (hybrid) zones, heterogeneities may survive at a smaller scale. Hence, even in highly dynamic conditions, domains in which the physical and chemical properties of the initial end-member magma are preserved are common in any mixed magmatic system, be it experimental (De Campos et al. 2011; Perugini et al. 2012; Laumonier et al. 2014a), numerical (Perugini et al. 2002; Petrelli et al. 2011) or natural (e.g. Barbarin 2005; Clemens et al. 2016; Janoušek et al. 2004; Kemp 2004; Perugini et al. 2003; Perugini and Poli 2012; Słaby and Martin 2008; Słaby et al. 2011a, b). This includes the Matok pluton, in which the two end-member magmas can still be identified at the outcrop scale as "coherent domains" (Bresler et al. 1997; Perugini et al. 2002), isolated by zones of hybrid composition (Fig. 3a). However, even in these hybrid domains, (pluri-)centimetric fragments of the mafic material in the felsic melt can still be identified (Fig. 3b); and the textural, chemical and isotopic data from apatites and titanites record the characteristics of the end-member magmas.

Despite this, some extent of chemical equilibration took place between the two magmas. This is indicated first by the limited spread of G- and B-type compositions in the PVA end-member proportion diagram (Fig. 11); and second by very minor inter-grain variations in Sr concentrations for both apatites (396 ± 39 ppm; 2 SD, $n = 88$) and titanites (40 ± 11 ppm; 2 SD, $n = 66$). The corresponding relative standard deviations for Sr (10–25%) are much smaller than for other elements such as trivalent cations (Y, REE) (75–150% for titanite and 100–250% for apatite). Therefore, Sr concentrations were completely equilibrated, not only at the scale of the grains (Fig. 6), but also among the whole population of apatite and titanites (i.e. at the scale of the hybrid sample); whereas REE-Y contents were not (a "diffusive fractionation" process, as observed in experimental results on element mobility during magma mixing; De Campos et al. 2011; Perugini et al. 2008, 2012). This suggests that chemical homogenization was largely controlled by diffusion between the two silicate liquids, which is at least an order of magnitude faster for Sr than for REE (Zhang et al. 2010).

This observation can be used to infer the timescales at which the liquid phases of the two mixed magmas remained in contact. This was done using a diffusion model based on Sr and Nd (Fig. 13b). Parameters controlling diffusion of trace elements in silicate melts include the degree of melt polymerization and H_2O contents (e.g. Baker 1991; Watson 1994; Mungall et al. 1999; Zhang et al. 2010). According to mineral assemblages and experimental results (Bogaerts et al. 2006), the water content in the Matok magmas ranged from ca. 1 to 5 wt% (Laurent et al. 2014c; Rapopo 2010). To bracket this range, we used two sets of diffusion coefficients for Sr and Nd calculated at 900 °C (equilibration temperature of the hybrid system, see above) using the experimentally determined Arrhenius parameters from a trachytic melt with 1.2–1.7 wt% H_2O (Behrens and Hahn 2009) and a wet haploandesite melt with 4.5–5.2 wt% H_2O (Koepke and Behrens 2001), both having SiO_2 contents (ca. 62 wt%) matching that of hybrid sample MAT-13. The values were used to calculate the extent of equilibration between the two magmas for different times at the scale of 2 cm (Fig. 13b), i.e. the average wavelength of chemical heterogeneities in active mixing zones (Fig. 3b). The extent of equilibration was defined as the ratio between the difference in concentration at a given time (expressed as xt_i) and the initial difference of concentration (expressed as X) (Fig. 13b).

The results show that for the H_2O-poor magma, the concentrations would be smoothed to less than 10% variation (insignificant within analytical uncertainties) in ca. 100 years for Sr (Fig. 13b). Although some extent of chemical homogenization did certainly take place for REE, it unlikely reached completion since apatites and titanites still preserve significant differences in REE

concentrations. PVA results indicate that variations in relative end-member proportions between B- and G-type apatite domains are in the range of 20–40%. Assuming accordingly that Nd homogenization between the two magmas did not exceed two-thirds of the initial concentration contrast, the maximum duration of chemical equilibration by diffusion is ca. 600 years (Fig. 13b). The timescales are one order of magnitude faster for the H_2O-rich magma: in that case, the chemical equilibration time should be comprised between 15 and 65 years (Fig. 13b). In summary, chemical diffusion between the two liquid phases of the mixed magmas lasted a few tens to a few hundred years at ca. 900 °C. This timescale is consistent with the preservation of REE zoning and lack of Sr zoning in MAT-13 apatite. At 900 °C, any Sr zoning within a spherical apatite with a radius of 50 μm would be indeed erased in ca. 30 months only (diffusion parameters from Cherniak and Ryerson 1993). In contrast, homogenization of Nd contents in the same grain would take nearly 5 Ma (diffusion parameters from Cherniak 2000).

The timescales of hybridization in Matok are much longer than those deduced from experimental studies of magma mixing, typically in the range of minutes to hours (De Campos et al. 2011; Perugini et al. 2012, 2015). However, these experiments are generally conducted at much higher (supraliquidus) temperatures (1200–1400 °C) and result in chemical heterogeneities at much smaller wavelengths (millimetric to sub-millimetric) than observed here, both considerably favouring chemical homogenization (Petrelli et al. 2011). Conversely, the complete hybridization of meter-sized enclaves within their host magmas in plutonic systems would require several hundred to one thousand years (Petrelli et al. 2006, 2011; Petrelli and Perugini 2014), in better agreement with our calculations. In any case, the inferred timescales (10s to 100s of years) for the Matok pluton are definitely shorter than the longevity of plutonic systems, i.e. typically several thousands, up to a few million years (Coleman et al. 2004; Michel et al. 2008; Nabelek et al. 2012; Menand et al. 2015). This shows that mechanical interactions and chemical exchanges between two magmas are fast processes relative to the lifetime of plutonic systems, even though the rheology contrast between the two magmas is minimal—as it is the case in the Matok pluton (Fig. 13a). Therefore, even in long-lived batholiths, complete magma hybridization may not be that common because it is fundamentally controlled by the particular thermal and mechanical conditions in the mixing zone.

Furthermore, despite the existence of diffusive fractionation processes at the sample scale, the bulk-rock sample MAT-13 does have a hybrid (chemical and isotopic) composition between the two end-members (see Fig. 2). This is because the length scale of sampling (hand specimen: 10s of centimeters) is greater than the remnant heterogeneities after mixing (centimetric or sub-centimetric). The extent of chemical equilibration in mixed magmatic systems is, therefore, an entirely subjective variable that depends on the observational length scales.

Conclusions

The results of this study, investigating the effect of magma mixing on textures, chemical and Sr–Nd isotopic compositions of apatites and titanites in a sample of the "hybridization zone" of the Matok pluton, lead to the following conclusions (also summarized in Supplementary Figure S1):

1. Most apatite crystals show concentric zoning in CL images, corresponding to abrupt variations in absolute concentrations of trace elements (especially REE and HFSE). In contrast, most titanites show little or no intra-grain, but large inter-grain chemical variations.

2. Apatite crystallized early during magma mixing, at high melt fraction and temperature (ca. 900–950 °C), enabling grain migration through melt domains with different composition. In contrast, titanite was formed at lower temperature (ca. 820–900 °C) in a crystal-richer mush containing melt pockets with compositions different from one another owing to various extent of magma mixing and Rayleigh fractionation.

3. Trace element constraints and PVA results suggest that the two mixed magmas were co-genetic. Those correspond, respectively, to a dioritic magma ($SiO_2 < 60$ wt%) and a granodioritic/granitic magma ($SiO_2 = 65–70$ wt%) both formed by different degrees of fractionation from similar, mantle-derived mafic melts. Therefore, magma mixing does not necessarily involve end-members from highly contrasted (crust vs. mantle) sources, but also can result from "self-mixing" of co-genetic magmas.

4. Significantly different εNd_t and $Sr_{(i)}$ value estimated in different apatite and titanite domains result from primary isotopic heterogeneities in the mantle source from which the parental mafic melts were derived. Such inhomogeneity is not resolved at the whole-rock scale, which emphasizes the importance of studying magma mixing from the mineral perspective.

5. Diffusive fractionation on hand-specimen scale between Sr (homogeneous concentrations in individual crystals and the whole population of apatites/titanites) and REE (significant intra-grain variations for apatites and inter-grain variations for titanites) requires that the chemical equilibration time at 900 °C (i.e. time during which the two liquid phases of the mixed magmas remained in contact) was comprised between 15–65 and 100–600 years.

6. The extent of chemical homogenization between two magmas is difficult to address because (1) it depends on the physical conditions of mixing (temperature, rheology, timescales); and (2) it is a "subjective" concept, depending on the considered system scale (outcrop, sample, mineral) and chemical element(s).

References

Altermann W, Lenhardt N (2012) The volcano-sedimentary succession of the Archean Sodium Group, Ventersdorp Supergroup, South Africa: volcanology, sedimentology and geochemistry. Precambr Res 214–215:60–81

Alves A, Janasi VDA, Simonetti A, Heaman L (2009) Microgranitic enclaves as products of self-mixing events: a study of open-system processes in the Maua Granite, São Paulo, Brazil, based on in situ isotopic and trace elements in plagioclase. J Petrol 50(12):2221–2247

Bacon CR (1986) Magmatic inclusions in silicic and intermediate volcanic rocks. J Geophys Res 91:6091–6112

Bacon CR (1989) Crystallization of accessory phases in magmas by local saturation adjacent to phenocrysts. Geochim Cosmochim Acta 53:1055–1066

Baker DR (1991) Interdiffusion of hydrous dacitic and rhyolitic melts and the efficacy of rhyolite contamination of dacitic enclaves. Contrib Miner Petrol 106:462–473

Barbarin B (1999) A review of the relationships between granitoid types, their origins and their geodynamic environments. Lithos 46:605–626

Barbarin B (2005) Mafic magmatic enclaves and mafic rocks associated with some granitoids of the central Sierra Nevada batholith, California: nature, origin, and relations with the hosts. Lithos 80:155–177

Barton JM Jr, Doig R, Smith CB, Bohlender F, van Reenen DD (1992) Isotopic and REE characteristics of the intrusive charnoenderbite and enderbite geographically associated with the Matok Pluton, Limpopo Belt, southern Africa. Precambr Res 55(1–4):451–467

Behrens H, Hahn M (2009) Trace element diffusion and viscous flow in potassium-rich trachytic and phonolitic melts. Chem Geol 259:63–77

Belousova EA, Walters S, Griffin WL, O'Reilly SY (2001) Trace element signatures of apatites in granitoids from the Mt Isa Inlier, northwestern Queensland. Aust J Earth Sci 48(4):603–619

Bogaerts M, Scaillet B, Vander Auwera J (2006) Phase equilibria of the Lyngdal granodiorite (Norway): implications for the origin of metaluminous ferroan granitoids. J Petrol 47(12):2405–2431

Bohlender F (1991) Igneous and metamorphic charnockitic rocks associated with the Matok pluton and their significance in the Limpopo orogeny. PhD thesis, Rand Afrikaans University, Johannesburg, South Africa

Bohlender F, Van Reenen DD, Barton JM Jr (1992) Evidence for metamorphic and igneous charnockites in the Southern Marginal Zone of the Limpopo Belt. Precambr Res 55(1–4):429–449

Bonin B (2004) Do coeval mafic and felsic magmas in post-collisional to within-plate regimes necessarily imply two contrasting, mantle and crustal, sources? A review. Lithos 78:1–24

Bresler L, Shinbrot T, Metcalfe G, Ottino JM (1997) Isolated mixing regions: origin, robustness and control. Chem Eng Sci 52:1623–1636

Bruand E, Storey C, Fowler M (2014) Accessory mineral chemistry of high Ba–Sr granites from Northern Scotland: constraints on petrogenesis and records of whole-rock signature. J Petrol 55(8):1619–1651

Castro A, De La Rosa JD, Stephens WE (1990) Magma mixing in the subvolcanic environment: petrology of the Gerena interaction zone near Seville, Spain. Contrib Miner Petrol 106:9–26

Castro A, Moreno-Ventas I, De La Rosa JD (1991) H-type (hybrid) granitoids: a proposed revision of the granite-type classification and nomenclature. Earth Sci Rev 31:237–253

Cherniak DJ (1995) Sr and Nd diffusion in titanite. Chem Geol 125(3–4):219–232

Cherniak DJ (2000) Rare earth element diffusion in apatite. Geochim Cosmochim Acta 64(22):3871–3885

Cherniak DJ, Ryerson FJ (1993) A study of strontium diffusion in apatite using Rutherford backscattering spectroscopy and ion implantation. Geochim Cosmochim Acta 57:4653–4662

Chu MF, Wang KL, Griffin WL, Chung SL, O'Reilly SY, Pearson NJ, Iizuka Y (2009) Apatite composition: tracing petrogenetic processes in Transhimalayan granitoids. J Petrol 50(10):1829–1855

Clemens JD, Darbyshire DPF, Flinders J (2009) Sources of post-orogenic calcalkaline magmas: the Arrochar and Garabal Hill–Glen Fyne complexes, Scotland. Lithos 112:524–542

Clemens JC, Stevens G, Farina F (2011) The enigmatic sources of I-type granites: the peritectic connexion. Lithos 126:174–181

Clemens JC, Regmi K, Nicholls IA, Weinberg R, Maas R (2016) The Tynong pluton, its mafic synplutonic sheets and igneous microgranular enclaves: the nature of the mantle connection in I-type granitic magmas. Contrib Miner Petrol 171:35

Coleman DS, Gray W, Glazner AF (2004) Rethinking the emplacement and evolution of zoned plutons: geochronologic evidence for incremental assembly of the Tuolumne Intrusive Suite. Calif Geol 32(5):433–436

Costa A, Caricchi L, Bagdassarov N (2009) A model for the rheology of particle-bearing suspensions and partially molten rocks. Geochem Geophys Geosyst 10(3):Q03010

Couch S, Sparks RSJ, Carroll MR (2001) Mineral disequilibrium in lavas explained by convective self-mixing in open magma chambers. Nature 411:1037–1039

Couzinie S, Laurent O, Moyen J-F, Zeh A, Bouilhol P, Villaros A (2016) Post-collisional magmatism: crustal growth not identified by zircon Hf–O isotopes. Earth Planet Sci Lett 456:182–195

Crank J (1975) The mathematics of diffusion, 2nd edn. Oxford University Press, London

Crow C, Condie KC (1988) Geochemistry and origin of the late Archean volcanics from the Ventersdorp Supergroup, South Africa. Precambr Res 42:19–37

De Campos CP, Perugini D, Ertel-Ingrisch W, Dingwell DB, Poli G (2011) Enhancement of magma mixing efficiency by chaotic dynamics: an experimental study. Contrib Miner Petrol 161:863–881

Dempster TJ, Jolivet M, Tubrett MN, Braithwaite CJR (2003) Magmatic zoning in apatite: a monitor of porosity and permeability change in granites. Contrib Miner Petrol 145:568–577

Didier J, Barbarin B (1991) Enclaves and granite petrology, Development in petrology, vol 13. Elsevier, Amsterdam

Druitt TH, Costa F, Deloule E, Dungan M, Scaillet B (2012) Decadal to monthly timescales of magma transfer and reservoir growth at a caldera volcano. Nature 482:77–80

Eglington BM, Armstrong RA (2004) The Kaapvaal Craton and adjacent orogens, southern Africa: a geochronological database and overview of the geological development of the craton. S Afr J Geol 107:13–32

Eichelberger JC (2010) Messy magma mixtures. Nat Geosci 3:593–594

Farina F, Stevens G, Dini A, Rocchi S (2012) Peritectic phase entrainment and magma mixing in the late Miocene Elba Island laccolith–pluton–dyke complex (Italy). Lithos 153:243–260

Fisher CM, McFarlane CRM, Hanchar JM, Schmitz MD, Sylvester PJ, Lam R, Longerich HP (2011) Sm–Nd isotope systematics by laser ablation-multicollector-inductively coupled plasma mass spectrometry: methods and potential natural and synthetic reference materials. Chem Geol 284:1–20

Foster GL, Vance D (2006) In situ Nd isotopic analysis of geological materials by laser ablation MC-ICP-MS. J Anal At Spectrom 21:288–296

Fujimaki H (1986) Partition-coefficients of Hf, Zr, and REE between zircon, apatite, and liquid. Contrib Miner Petrol 94(1):42–45

Giordano D, Russel JK, Dingwell DB (2008) Viscosity of magmatic liquids: a model. Earth Planet Sci Lett 271:123–134

Glazner AF, Bartley JM, Coleman DS, Gray W, Taylor ZT (2004) Are plutons assembled over millions of years by amalgamation from small magma chambers? GSA Today 14:4–11

Graham CM, Elphick SC (1990) A re-examination of the role of hydrogen in Al–Si interdiffusion in feldspars. Contrib Miner Petrol 104:481–491

Green TH, Pearson NJ (1986) Rare-earth element partitioning between sphene and coexisting silicate liquid at high-pressure and temperature. Chem Geol 55:105–119

Harrison TM, Watson EB (1984) The behavior of apatite during crustal anatexis: Equilibrium and kinetic considerations. Geochim Cosmochim Acta 48:1467–1477

Hayden LA, Watson EB, Wark DA (2008) A thermobarometer for sphene (titanite). Contrib Miner Petrol 155:529–540

Hodson ME, Finch AA (1997) Trough structures in the Western syenite of Kûngnât, S Greenland: mineralogy and mechanism of formation. Contrib Miner Petrol 127:46–56

Holness MB, Martin VM, Pyle DM (2005) Information about open-system magma chambers derived from textures in magmatic enclaves: the Kameni Islands, Santorini, Greece. Geol Mag 142:637–649

Jacobsen SB, Wasserburg GJ (1984) Sm–Nd isotopic evolution of chondrites and achondrites, II. Earth Planet Sci Lett 67(2):137–150

Janoušek V, Braithwaite CJR, Bowes DR, Gerdes A (2004) Magma-mixing in the genesis of Hercynian calc-alkaline granitoids: an integrated petrographic and geochemical study of the Sázava intrusion, Central Bohemian Pluton, Czech Republic. Lithos 78:67–99

Jellinek AM, Kerr RC (1999) Mixing and compositional stratification produced by natural convection. 2. Applications to the differentiation of basaltic and silicic magma chambers and komatiite lava flows. J Geophys Res 104(B4):7203–7218

Jennings ES, Marschall HR, Hawkesworth CJ, Storey CD (2011) Characterization of magma from inclusions in zircon: apatite and biotite work well, feldspar less so. Geology 39(9):863–866

Johnston AD, Wyllie PJ (1988) Constraints on the origin of Archean trondhjemites based on phase relationship of Nûk gneiss with H_2O at 15 kbar. Contrib Miner Petrol 100:35–46

Karsli O, Dokuz A, Uysal I, Aydin F, Chen B, Kandemir R, Wijbrans J (2010) Relative contributions of crust and mantle to generation of Campanian high-K calc-alkaline I-type granitoids in a subduction setting, with special reference to the Harsit Pluton, Eastern Turkey. Contrib Miner Petrol 160:467–487

Kemp AIS (2004) Petrology of high-Mg, low-Ti igneous rocks of the Glenelg River Complex (SE Australia) and the nature of their interaction with crustal melts. Lithos 78:119–156

Kemp AIS, Hawkesworth CJ (2003) Granitic perspectives on the generation and secular evolution of the continental crust. In: Rudnick RL (ed) The crust. Treatise on geochemistry. Elsevier-Pergamon, Oxford, pp 349–410

Kempe U, Götze J (2002) Cathodoluminescence (CL) behaviour and crystal chemistry of apatite from rare-metal deposits. Mineral Mag 66(1):151–172

Koepke J, Behrens H (2001) Trace element diffusion in andesitic melts: an application of synchrotron X-ray fluorescence analysis. Geochim Cosmochim Acta 65:1481–1498

Kramers JD, Henzen M, Steidle L (2014) Greenstone belts at the northernmost edge of the Kaapvaal Craton: timing of tectonic events and a possible crustal fluid source. Precambr Res 253:96–113

Kreissig K, Nagler TF, Kramers JD, Van Reenen DD, Smit CA (2000) An isotopic and geochemical study of the Kaapvaal Craton and the Southern Marginal Zone of the Limpopo belt: are they juxtaposed terranes? Lithos 50:1–25

Kreissig K, Holzer L, Frei R, Villa IM, Kramers JD, Smit CA, Van Reenen DD (2001) Geochronology of the Hout River Shear Zone and the metamorphism in the Southern Marginal Zone of the Limpopo Belt, Southern Africa. Precambr Res 109:145–173

Kronenberg AK, Yund RA, Rossman GR (1996) Stationary and mobile hydrogen defects in potassium feldspar. Geochim Cosmochim Acta 60:4075–4094

Laumonier M, Scaillet B, Arbaret L, Champallier R (2014a) Experimental simulation of magma mixing at high pressure. Lithos 196:281–300

Laumonier M, Scaillet B, Pichavant M, Champallier R, Andujar J, Arbaret L (2014b) On the conditions of magma mixing and its bearing on andesite production in the crust. Nat Commun 5:5607

Laurent O (2012) Les changements géodynamiques à la transition Archéen-Protérozoïque: étude des granitoïdes de la marge Nord du craton du Kaapvaal (Afrique du Sud). Unpublished PhD thesis, University Blaise Pascal, Clermont-Ferrand II **(in French)**

Laurent O, Zeh A (2015) A linear Hf isotope-age array despite different granitoid sources and complex Archean geodynamics: example from the Pietersburg block (South Africa). Earth Planet Sci Lett 430:326–338

Laurent O, Doucelance R, Martin H, Moyen JF (2013a) Differentiation of the late-Archaean sanukitoid series and some implications for crustal growth: insights from geochemical modelling on the Bulai pluton, Central Limpopo Belt, South Africa. Precambr Res 227:186–203

Laurent O, Paquette J-L, Martin H, Doucelance R, Moyen J-F (2013b) LA-ICP-MS dating of zircons from Meso- and Neoarchean granitoids of the Pietersburg block (South Africa): crustal evolution at the northern margin of the Kaapvaal craton. Precambr Res 230:209–226

Laurent O, Martin H, Moyen J-F, Doucelance R (2014a) The diversity and evolution of late-Archean granitoids: Evidence for the onset of "modern-style" plate tectonics between 3.0 and 2.5 Ga. Lithos 205:208–235

Laurent O, Nicoli G, Zeh A, Stevens G, Moyen J-F, Vezinet A et al (2014b) Comment on "Ultrahigh temperature granulites and magnesian charnockites: evidence for the Neoarchean accretion along the northern margin of the Kaapvaal Craton" by Rajesh. Precambr Res 255:455–458

Laurent O, Rapopo M, Stevens G, Moyen J-F, Martin H, Doucelance R, Bosq C (2014c) Contrasting petrogenesis of Mg–K and Fe–K granitoids and implications for post-collisional magmatism: case

study from the late-Archean Matok pluton (Pietersburg block, South Africa). Lithos 196:131–149

Lisowiec K, Słaby E, Förster HJ (2015) Polytopic vector analysis (PVA) modelling of whole-rock and apatite chemistry from the Karkonosze composite pluton (Poland, Czech Republic). Lithos 230:105–120

Luhr JF, Carmichael ISE, Varekamp JC (1984) The 1982 eruptions of El Chichón Volcano, Chiapas, Mexico: mineralogy and petrology of the anhydritebearing pumices. J Volcanol Geotherm Res 23(1–2):69–108

Maas R, Nicholls IA, Legg C (1997) Igneous and metamorphic enclaves in the S-type Deddick Granodiorite, Lachlan Fold Belt, SE Australia: petrographic, geochemical and Nd–Sr isotopic evidence for crustal melting and magma mixing. J Petrol 38(7):815–841

McLeod GW, Dempster TJ, Faithfull JW (2011) Deciphering magma-mixing processes using zoned titanite from the Ross of Mull Granite, Scotland. J Petrol 52:55–82

Menand T, Annen C, de Saint-Blanquat M (2015) Rates of magma transfer in the crust: insights into magma reservoir recharge and pluton growth. Geology 43(3):199–202

Michel J, Baumgartner L, Putlitz B, Schaltegger U, Ovtcharova M (2008) Incremental growth of the Patagonian Torres del Paine laccolith over 90 k.y. Geology 36:459–462

Miles AJ, Graham CM, Hawkesworth CJ, Gillespie MR, Hinton RW (2013) Evidence for distinct stages of magma history recorded by the compositions of accessory apatite and zircon. Contrib Miner Petrol 166:1–19

Moyen JF, Martin H, Jayananda M (2001) Multi-element geochemical modelling of crust–mantle interactions during late-Archaean crustal growth: the Closepet granite (South India). Precambr Res 112:87–105

Mungall JE, Dingwell DB, Chaussidon M (1999) Chemical diffusivities of 18 trace elements in granitoid melts. Geochim Cosmochim Acta 63:2599–2610

Murphy MD, Sparks RSJ, Barclay J, Carroll MR, Lejeune A-M, Brewer TS, Macdonald R, Black S, Young S (1998) The role of magma mixing in triggering the current eruption at the Soufriere Hills volcano, Montserrat, West Indies. Geophys Res Lett 25(18):3433–3436

Nabelek PI, Hofmeister AM, Whittington AG (2012) The influence of temperature-dependent thermal diffusivity on the conductive cooling rates of plutons and temperature-time paths in contact aureoles. Earth Planet Sci Lett 317–318:157–164

Nagasawa H (1970) Rare earth concentrations in zircon and apatite and their host dacite and granites. Earth Planet Sci Lett 9:359–364

Nagasawa H, Schnetzler CC (1971) Partitioning of rare earth, alkali, and alkaline earth elements between phenocrysts and acidic igneous magmas. Geochim Cosmochim Acta 35:953–968

Neuser RD, Bruhn F, Götze J, Habermann D, Richter DK (1995) Kathodolumineszenz: Methodik und Anwendung. Zentralblatt für Geologie und Paläontologie Teil I(1/2):287–306

Oldenburg CM, Spera FJ, Yuen DA, Sewell G (1989) Dynamic mixing in magma bodies: theory, simulations and implications. J Geophys Res 94:9215–9236

Ottino JM (1989) The kinematics of mixing: stretching, chaos and transport. Cambridge University Press, Cambridge

Perugini D, Poli G (2001) Chaotic dynamics and fractals in magmatic interaction processes: a different approach to the interpretation of mafic microgranular enclaves. Earth Planet Sci Lett 175:93–103

Perugini D, Poli G (2004) Determination of the degree of compositional disorder in magmatic enclaves using SEM, X-ray element, maps. Eur J Mineral 16:431–442

Perugini D, Poli G (2012) The mixing of magmas in plutonic and volcanic environments: analogies and differences. Lithos 153:261–277

Perugini D, Poli G, Prosperini N (2002) Morphometric analysis of magmatic enclaves: a tool for understanding magma vesiculation and ascent. Lithos 61:225–235

Perugini D, Poli G, Christofides G, Eleftheriadis G (2003) Magma mixing in the Sithonia Plutonic Complex, Greece: evidence from mafic microgranular enclaves. Mineral Petrol 78:173–200

Perugini D, Poli G, Valentini L (2005) Strange attractors in plagioclase oscillatory zoning: petrological implications. Contrib Miner Petrol 149:482–497

Perugini D, Petrelli M, Poli G (2006) Diffusive fractionation of trace elements by chaotic mixing of magmas. Earth Planet Sci Lett 243:669–680

Perugini D, De Campos CP, Dingwell DB, Petrelli M, Poli G (2008) Trace element mobility during magma mixing: preliminary experimental results. Chem Geol 256:146–157

Perugini D, De Campos CP, Ertel-Ingrisch W, Dingwell DB (2012) The space and time complexity of chaotic mixing of silicate melts: Implications for igneous petrology. Lithos 155:326–340

Perugini D, De Campos CP, Petrelli M, Dingwell DB (2015) Concentration variance decay during magma mixing: a volcanic chronometer. Sci Rep 5:14225

Petrelli M, Perugini D (2014) Unravelling the time-scales of magma mixing: petrological and volcanological implications. In: American Geophysical Union, fall meeting 2014, Abstract #V33A-4839

Petrelli M, Perugini D, Poli G (2006) Time-scales of hybridisation of magmatic enclaves in regular and chaotic flow fields: petrologic and volcanologic implications. Bull Volcanol 68:285–293

Petrelli M, Perugini D, Poli G (2011) Transition to chaos and implications for timescales of magma hybridization during mixing processes in magma chambers. Lithos 125:211–220

Piccoli PH, Candela PA (1994) Apatite in felsic rocks: a model for the estimation of initial halogen concentrations in the Bishop Tuff (Long Valley) and Tuolumne Intrusive Suite (Sierra Nevada Batholith) magmas. Am J Sci 294:92–135

Pietranik A, Koepke J (2009) Interactions between dioritic and granodioritic magmas in mingling zones: plagioclase record of mixing, mingling and subsolidus interactions in the Gęsiniec Intrusion, NE Bohemian Massif, SW Poland. Contrib Miner Petrol 158:17–36

Pietranik A, Storey C, Dhuime B, Tyszka R, Whitehouse M (2011) Decoding whole rock, plagioclase, zircon and apatite isotopic and geochemical signatures from variably contaminated dioritic magmas. Lithos 127:455–467

Pin C, Binon M, Belin J-M, Barbarin B, Clemens JD (1990) Origin of microgranular enclaves in granitoids: equivocal Sr–Nd evidence from Hercynian rocks in the Massif Central (France). J Geophys Res 95(B11):17821–17828

Poli G, Tommasini S, Halliday AN (1996) Trace elements and isotopic exchange during acid–basic magma interaction processes. Trans R Soc Edinb Earth Sci 87:225–232

Poujol M, Robb LJ, Anhaeusser CR, Gericke B (2003) A review of the geochronological constraints on the evolution of the Kaapvaal Craton, South Africa. Precambr Res 127(1–3):181–213

Prowatke S, Klemme S (2005) Effect of melt composition on the partitioning of trace elements between titanite and melt. Geochim Cosmochim Acta 69:695–709

Prowatke S, Klemme S (2006a) Rare earth element partitioning between titanite and silicate melts: Henry's law revisited. Geochim Cosmochim Acta 70:4997–5012

Prowatke S, Klemme S (2006b) Trace element partitioning between apatite and silicate melts. Geochim Cosmochim Acta 70:4513–4527

Rajesh HM, Santosh M, Wan Y, Liu D, Liu SJ, Belyanin GA (2014) Ultrahigh temperature granulites and magnesian charnockites: evidence for Neoarchean accretion along the northern margin of the Kaapvaal Craton. Precambr Res 246:150–159

Rao NVC, Wu FY, Srinivas M (2012) Mesoproterozoic emplacement and enriched mantle derivation of the Racherla alkali syenite, Palaeo-Mesoproterozoic Cuddapah Basin, southern India: insights from in situ Sr–Nd isotopic analysis on apatite. Geol Soc Lond Spec Publ 365:185–195

Rapopo M (2010) Petrogenesis of the Matok pluton, South Africa: implications on the heat source that induced regional metamorphism in the Southern Marginal Zone of the Limpopo Belt. MSc thesis, University of Stellenbosch, South Africa

Reubi O, Blundy J (2009) A dearth of intermediate melts at subduction zone volcanoes and the petrogenesis of arc andesites. Nature 461:1269–1273

Ruprecht P, Bachmann O (2010) Pre-eruptive reheating during magma mixing at Quizapu volcano and the implications for the explosiveness of silicic arc volcano. Geology 38(10):919–922

Sawka WN, Chappell BW, Norrish K (1984) Light-rare-earth-element zoning in sphene and allanite during granitoid fractionation. Geology 12:131–134

Schmidt MW, Thompson AB (1996) Epidote in calc-alkaline magmas: an experimental study of stability, phase relationships, and the role of epidote in magmatic evolution. Am Miner 81:462–474

Sha L-K, Chappell BW (1999) Apatite chemical composition, determined by electron microprobe and laser-ablation inductively coupled plasma mass spectrometry, as a probe into granite petrogenesis. Geochim Cosmochim Acta 63:3861–3881

Słaby E, Martin H (2008) Mafic and felsic magma interaction in granites: the Hercynian Karkonosze Pluton (Sudetes, Bohemian Massif). J Petrol 49(2):353–391

Słaby E, Götze J, Wörner G, Simon K, Wrzalik R, Śmigielski M (2008) K-feldspar phenocrysts in microgranular magmatic enclaves: a cathodoluminescence and geochemical study of crystal growth as a marker of magma mingling dynamics. Lithos 105:85–97

Słaby E, Götze J, Wörner G, Simon K, Wrzalik R, Śmigielski M (2010) K-feldspar phenocrysts in microgranular magmatic enclaves: a cathodoluminescence and geochemical study of crystal growth as a marker of magma mingling dynamics. Lithos 105:85–97

Słaby E, Martin H, Hamada M, Śmigielski M, Domonik A, Götze J, Hoefs J, Hałas S, Simon K, Devidal JL, Moyen JF, Jayananda M (2011a) Evidence in Archaean alkali feldspar megacrysts for high-temperature interaction with mantle fluids. J Petrol. doi:10.1093/petrology/egr056

Słaby E, Śmigielski M, Śmigielski T, Domonik A, Simon K, Kronz A (2011b) Chaotic three-dimensional distribution of Ba, Rb, and Sr in feldspar megacrysts grown in an open magmatic system. Contrib Miner Petrol 162:909–927

Słaby E, De Campos CP, Majzner K, Simon K, Gros K, Moszumanska I, Jokubauskas P (2017) Feldspar megacrysts from the Santa Angélica composite pluton—Formation/transformation path revealed by combined CL, Raman and LA-ICP-MS data. Lithos 277:269–283

Smit CA, van Reenen DD, Roering C (2014) Role of fluids in the exhumation of the Southern Marginal Zone of the Limpopo Complex, South Africa. Precambr Res 253:81–95

Sparks SRJ, Marshall LA (1986) Thermal and mechanical constraints on mixing between mafic and silicic magmas. J Volcanol Geotherm Res 29:99–124

Sparks SRJ, Sigurdsson H, Wilson L (1977) Magma mixing: a mechanism for triggering acid explosive eruptions. Nature 267:315–318

Spera FJ, Schmidt JS, Bohrson WA, Brown GA (2016) Dynamics and thermodynamics of magma mixing: insights from a simple exploratory model. Am Miner 101:627–643

Sun JF, Yang JH, Wu FY, Li XH, Yang YH, Xie LW, Wilde SA (2010) Magma mixing controlling the origin of the Early Cretaceous Fangshan granitic pluton, North China Craton: in situ U–Pb age and Sr-, Nd-, Hf- and O-isotope evidence. Lithos 120:421–438

Tepper JH, Kuehner SM (1999) Complex zoning in apatite from the Idaho batholith: a record of magma mixing and intracrystalline trace element diffusion. Am Miner 84:581–595

Tiepolo M, Oberti R, Vannucci R (2002) Trace-element incorporation in titanite: constraints from experimentally determined solid/liquid partition coefficients. Chem Geol 191:105–119

Vantongeren JA, Mathez EA (2013) Incoming magma composition and style of recharge below the pyroxenite marker, eastern Bushveld complex, South Africa. J Petrol 54:1585–1605

Villaros A, Stevens G, Moyen J-F, Buick IS (2009) The trace element compositions of S-type granites: evidence for disequilibrium melting and accessory phase entrainment in the source. Contrib Miner Petr 158(4):543–561

Vroon PZ, van der Wagt B, Koornneef JM, Davies GR (2008) Problems in obtaining precise and accurate Sr isotope analysis from geological materials using laser ablation MC-ICPMS. Anal Bioanal Chem 390:465–476

Watson EB (1994) Diffusion in volatile-bearing magmas. Rev Mineral 30:371–411

Watson EB, Green TH (1981) Apatite/liquid partition coefficients for the rare-earth elements and strontium. Earth Planet Sci Lett 56:405–421

Watson EB, Liang Y (1995) A simple model for sector zoning in slowly grown crystals: implications for growth rate and lattice diffusion, with emphasis on accessory minerals in crustal rocks. Am Miner 80:1179–1187

Wiebe RA, Blair KD, Hawkins DP, Sabine CP (2002) Mafic injections, in situ hybridization, and crystal accumulation in the Pyramid Peak granite, California. GSA Bull 114(7):909–920

Wiebe RA, Wark DA, Hawkins DP (2007) Insights from quartz cathodoluminescence zoning into crystallization of the Vinalhaven granite, coastal Maine. Contrib Miner Petrol 154:439–453

Wilcox RE (1999) The idea of magma mixing: history of a struggle for acceptance. J Geol 107:421–432

Williamson B, Downes H, Thirlwall M, Beard A (1997) Geochemical constraints on restite composition and unmixing in the Velay anatectic granite, French Massif Central. Lithos 40(2–4):295–319

Workman RK, Hart SR (2005) Major and trace element composition of the depleted MORB mantle (DMM). Earth Planet Sci Lett 231(1–2):53–72

Yang YH, Wu FY, Yang JH, Chew DM, Xie LW, Chu ZY, Zhang YB, Huang C (2014) Sr and Nd isotopic compositions of apatite reference materials used in U–Th–Pb geochronology. Chem Geol 385:35–55

Zeh A, Gerdes A, Barton JM Jr (2009) Archean accretion and crustal evolution of the Kalahari Craton—the zircon age and Hf isotope record of granitic rocks from Barberton/Swaziland to the Francistown Arc. J Petrol 50:933–966

Zhang Y, Ni H, Chen Y (2010) Diffusion data in silicate melts. Rev Mineral Geochem 72:311–408

Zirner ALK, Marks MAW, Wenzel T, Jacob DE, Markl G (2015) Rare earth elements in apatite as a monitor of magmatic and metasomatic processes: the Ilímaussaq complex, South Greenland. Lithos 228–229:12–22